Dynamic *in situ* confinement triggers ligand-free neuropeptide receptor signaling

M. Florencia Sánchez[1], Marina S. Dietz[2], Ulrike Müller[3], Julian Weghuber[3,4], Karl Gatterdam[1], Ralph Wieneke[1], Mike Heilemann[2], Peter Lanzerstorfer[3], Robert Tampé[1,*]

[1]Institute of Biochemistry, Biocenter, Goethe University Frankfurt, Max-von-Laue-Str. 9, 60438 Frankfurt am Main, Germany; [2]Institute of Physical and Theoretical Chemistry, Goethe University Frankfurt, Max-von-Laue-Str. 7, 60438 Frankfurt am Main, Germany; [3]School of Engineering and Environmental Sciences, University of Applied Sciences Upper Austria, Wels, Austria; [4]FFoQSI - Austrian Competence Centre for Feed and Food Quality, Safety & Innovation, FFoQSI GmbH, Technopark 1D, 3430 Tulln, Austria

*To whom correspondence may be addressed Email: tampe@em.uni-frankfurt.de

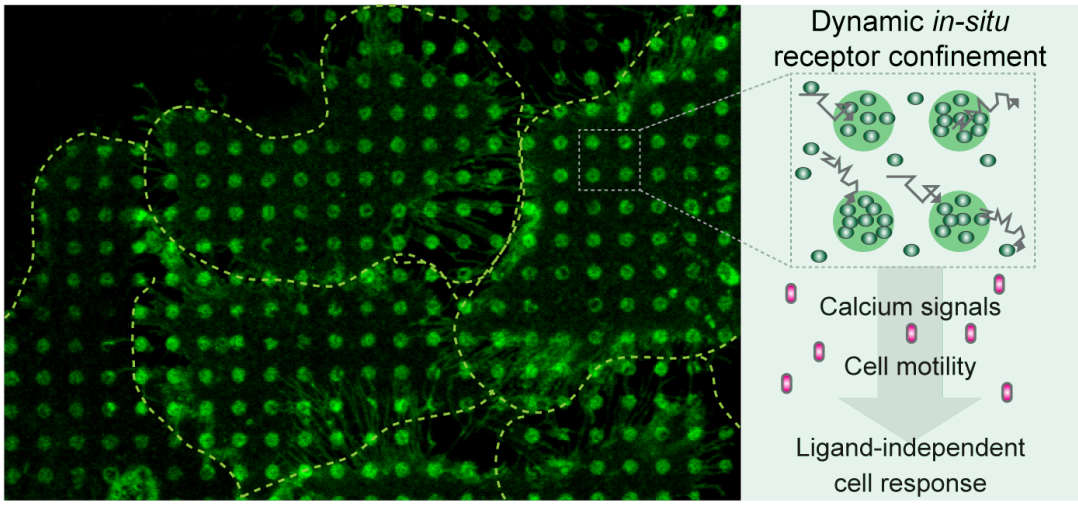

Abstract

Membrane receptors are central to cell-cell communication. Receptor clustering at the plasma membrane modulates physiological responses, and microscale receptor organization is critical for downstream signaling. Spatially restricted cluster formation of the neuropeptide Y_2 hormone receptor (Y_2R) was observed *in vivo*; however, the relevance of this confinement is not fully understood. Here, we controlled Y_2R clustering *in situ* by a multivalent chelator nanotool in prestructured matrices. Fast Y_2R enrichment in microscale arrays triggered a ligand-independent downstream signaling determined by an increase in cytosolic calcium, cell spreading and migration. We reveal that ligand-independent signaling by confinement differs from ligand-induced activation in the recruitment of arrestin-3 as downstream effector, which was recruited to confined regions only in presence of the ligand. The employed multivalent nanotool facilitated a dynamic receptor enrichment with high exchange in the confined regions, comparable to microscale condensates. This concept enables *in situ* organization of membrane receptors and the exploration of ligand-independent receptor signaling.

Keywords: G protein-coupled receptors / membrane organization / membrane proteins / phase segregation / receptor clustering

Introduction

Cells translate stimuli into biochemical signals through membrane receptors controlling multiple aspects of cell behavior, including migration (Kupperman *et al.*, 2000; Stallaert *et al.*, 2018), differentiation (Li & Rudensky, 2016; Luther & Cyster, 2001), apoptosis (Scott *et al.*, 2009), as well as infectious diseases and cancer (Boncompain *et al.*, 2019; Haqshenas & Doerig, 2019; Kawai & Akira, 2005; Pasquale, 2010; Pike *et al.*, 2018; Sebestyen *et al.*, 2020; Tsukiyama *et al.*, 2020). Receptors form dynamic assemblies, condensates, or clusters that modulate downstream signaling and thus the final physiological response. Upon activation, these receptors undergo transitions from freely diffusing monomers to less mobile nanoclusters and further to higher-order oligomers (Ojosnegros *et al.*, 2017; Su *et al.*, 2016). Recently, liquid-liquid phase separation (LLPS) has been considered as a general mechanism for higher-order receptor cluster formation. In these dynamic, liquid-like condensates driven by weak multivalent interactions, the likelihood of receptor activation increases as neighboring molecules can act together engaging ligands (Case *et al.*, 2019; Lyon *et al.*, 2021). In signal transduction, the mechanisms for receptor cluster formation and cluster behavior have become physiologically relevant topics. However, the role of mesoscale (hundreds of nanometers) receptor organization in signal transduction remains unsolved, mainly because concepts to trigger and analyze receptor clustering *in situ* are largely limited.

Nano- and microlithographic approaches have provided cell-compatible scaffolds to investigate confined ligand-receptor interactions (Manz & Groves, 2010; Nair *et al.*, 2011; Torres *et al.*, 2008). Various techniques, ranging from photolithography to polymer lift-off and microcontact printing (μCP), have yielded information on how topology and mobility of the stimulus regulate cell responses (Bernard *et al.*, 2000; Doh & Irvine, 2006; Mossman *et al.*, 2005; Sánchez *et al.*, 2018; Traub *et al.*, 2016). So far, these methods utilize receptor ligands or antibodies to induce a rather static cluster formation. However, fast dynamic signaling at the plasma membrane requires tools that enable receptor clustering in a fast, specific, and *in situ* intervention of receptor networks.

60 Heterotrimeric guanine nucleotide-binding protein (G protein)-coupled receptors (GPCR)
61 are key cell surface proteins that regulate a plethora of cellular responses to external stimuli
62 (Rosenbaum *et al.*, 2009; Venkatakrishnan *et al.*, 2013; Wootten *et al.*, 2018). The Y_2 receptor
63 (Y_2R) is one of the four human neuropeptide Y (NPY) receptor subtypes, which belong to the
64 rhodopsin-like (class A) GPCR superfamily (Parker & Balasubramaniam, 2008; Tang *et al.*,
65 2021). Y_2R is linked to many important physiological processes, such as fear extinction
66 (Méndez-Couz *et al.*, 2021), regulation of food intake (Huang *et al.*, 2014), and obesity
67 (Lafferty *et al.*, 2021). Y_2R activation by neuropeptide Y (NPY) has been shown to promote
68 cell migration and proliferation (Ekstrand *et al.*, 2003; Movafagh *et al.*, 2006). Recently, we
69 demonstrated that Y_2Rs respond to light-guided microscale clustering at spatially defined
70 locations (Sánchez *et al.*, 2021). Y_2Rs are activated independently of the presence of the
71 canonical ligand, evoking an increase in cytosolic calcium, a change in cell spreading
72 behavior, and a localized migratory pattern.
73 Here, we established a versatile concept for *in situ* receptor clustering using a multivalent
74 chelator nanotool (*tris N*-nitrilotriacetic acid, *tris*NTA), which displays high affinity for histidine
75 (His)-tagged proteins. The small size of the chelator tool in combination with a prestructured
76 platform enabled high-content receptor clustering with high spatiotemporal resolution. The
77 lateral organization of Y_2Rs in living cells was controlled within minutes in a non-invasive
78 ("traceless") and ligand-free manner. Microscale receptor condensates with a high degree of
79 homogeneity in size and density were generated in the plasma membrane. Receptor
80 clustering triggered ligand-independent activation of signal transduction, as evidenced by an
81 increase in cytosolic calcium and cell motility. By evaluating arrestin-3 (Arr3) recruitment as a
82 downstream signaling event, we uncovered high Arr3 co-recruitment to the patterned areas
83 only in the presence of the canonical ligand, suggesting an Arr3-independent desensitization
84 mechanism for the ligand-independent response. Strikingly, analysis of the receptor mobility
85 revealed a dynamic receptor assembly with high exchange within the confined areas, showing
86 similarities to liquid-like condensates. The versatility of this generic approach may advance
87 studies of ligand-free receptor signaling by dynamic confinement.

88 **Results**

89 **High-content receptor clustering in living cells**

90 We developed a system to induce dynamic receptor assembly *in situ* based on a multivalent
91 chelator *tris*NTA nanotool (Fig 1A), which is equipped with a biotin moiety (*tris*NTA$^{PEG12-B}$)
92 (Fig 1B). *tris*NTA$^{PEG12-B}$ displays a high affinity for His$_6$-tagged proteins ($K_D \approx 10$ nM), resulting
93 in a site-specific but reversible interaction (Gatterdam *et al.*, 2018). Microcontact printing is a
94 widely used method to investigate protein-protein interactions in living cells (Bernard *et al.*,
95 2000; Torres *et al.*, 2008). However, patterned substrates with a generic structure allowing
96 high-content analyses of cells are difficult to produce. We used a large-area perfluoropolyether
97 (PFPE) elastomeric stamps inked with bovine serum albumin (BSA) to print 96-well size glass
98 (Hager *et al.*, 2021; Lanzerstorfer *et al.*, 2020). Wells within these plates containing a BSA-
99 structured matrix were functionalized with biotinylated BSA (biotin-BSA) and streptavidin (SA)
100 (Fig 1A). Subsequent functionalization with the nanotool and His$_6$-tagged fluorescent proteins,
101 resulted in well-resolved protein patterns that were analyzed by confocal laser scanning
102 microscopy (CLSM). This confirmed the specificity of the nickel-loaded *tris*NTA chelator to
103 capture His$_6$-tagged proteins in defined regions of 1 µm or 3 µm diameter (Fig 1C, D).

104 The ability to control the organization of membrane receptors in real time is important for
105 dissecting the spatial complexity of cell signaling and the extracellular environment. To this
106 end, we utilized a tetracycline-inducible (T-Rex) expression system to establish a monoclonal
107 human cervical cancer HeLa cell line expressing low amounts of the Y_2R (~300,000
108 receptors/cell) (Sánchez *et al.*, 2021). Y_2Rs displayed an N-terminal His$_6$-tag to the
109 extracellular space and a cytosolic, C-terminal monomeric Enhanced Green Fluorescent
110 Protein (mEGFP) (His$_6$-Y_2R^{mEGFP}, in brief Y_2R). It is worth mentioning that these modifications
111 do not affect receptor activity, selectivity, or ligand binding as demonstrated (Sánchez *et al.*,
112 2021). In addition, studies determined that Y_2R does not need the N-terminus for ligand
113 binding (Lindner *et al.*, 2009). Y_2R-positive cells properly adhered to 1 µm and 3 µm SA-
114 functionalized matrices and showed a homogeneous receptor distribution at the basal plasma

115 membrane (Fig 1E). Addition of *tris*NTA$^{PEG12-B}$ (100 nM final) triggered receptor assembly.
116 Within five minutes, all cells showed receptor patterns at the plasma membrane comparable
117 in size and density (Fig 1E, F, Fig EV1). Importantly, recruitment of soluble His$_6$-tagged GFP
118 proteins as well as Y_2Rs to 1 µm prestructured spots led to analogous intensity profiles,
119 reflecting that similar densities were obtained in both cases (Fig 1D, G). In contrast, cells
120 expressing Y_2Rs lacking the His$_6$-tag (Y_2R^{mEGFP}) showed no receptor clustering after addition
121 of *tris*NTA$^{PEG12-B}$ (Fig EV2), demonstrating the specificity of the His$_6$-tag/*tris*NTA interaction in
122 living cells. Remarkably, ten minutes after receptor clustering by the multivalent nanotool, the
123 Y_2R enrichment resulted in an integrated receptor density equivalent to that of cells cultured
124 on matrices functionalized with anti-His$_6$ antibodies. However, a tenfold higher antibody
125 concentration (1 µM) was required compared to the multivalent nanotool, demonstrating its
126 efficacy in capturing His$_6$-tagged membrane receptors (Fig EV3). The 3 µm diameter
127 nanotool-induced receptor clusters presented a ninefold increase in integrated density
128 compared to 1 µm arrays, consistent with the increase in pattern area (Fig EV3). Overall, our
129 approach enabled versatile *in situ* receptor organization with high specificity.
130

131 **Ligand-independent receptor clustering triggers fast signaling**

132 To follow receptor clustering *in situ*, Y_2R-expressing cells were cultured on microstructured
133 matrices with a diameter of 1 µm, the smallest pattern we can produce and analyze with high
134 accuracy. After addition of the multivalent nanotool, the receptor redistribution was tracked by
135 confocal microscopy. Receptor clustering occurred in the first minutes and increased steadily
136 within 10 min, resulting in a twofold increase in receptor density compared to the initial state
137 (Fig 2A, Movie 1). Considering the average cell area of 1,420 ± 50 µm^2 (n = 66 cells) and the
138 enrichment factor (twofold), we estimated a receptor density of ~400 receptors/µm^2 in the
139 patterned regions (~300 receptors per 1 µm spot), a value comparable to other receptor
140 studies utilizing Fluorescence Correlation Spectroscopy methods (Bag *et al.*, 2015; Chen *et*
141 *al.*, 2009). The kinetic profile for Y_2R recruitment to the 1 µm spots followed a pseudo-first-
142 order assembly rate of 0.20 ± 0.03 min^{-1} (Fig 2A, C). Despite of the high affinity and kinetically

143 stable binding (k_{off} = 0.18 h^{-1}) (Gatterdam *et al.*, 2018), the His-tag/*tris*NTA system relies on
144 molecular multivalency, which enables competition of the binding sites with histidine, thus
145 making the process of receptor assembly reversible. Addition of histidine to patterned cells led
146 to the disassembly of the receptor clusters in a rapid and complete manner, demonstrating a
147 key advantage of the approach to investigate receptor dynamics (Fig 2B).

148 Upon receptor clustering by the multivalent interaction nanotool, we observed a fast change
149 in cell spreading and motility. Analysis of cell spreading revealed a 20% increase in the total
150 cell area concomitant to receptor assembly (Fig 2A, D, Fig 3A), indicating ligand-independent
151 receptor activation upon clustering. Cells cultured on matrices in the absence of SA as well as
152 cells expressing Y_2R^{mEGFP} (lacking a His_6-tag) on SA-matrices showed no significant change
153 in cell spreading upon addition of the *tris*$NTA^{PEG12-B}$ (Fig EV4). As calcium signals are widely
154 known to regulate cell motility, we monitored local calcium dynamics utilizing a far-red cell-
155 permeable Ca^{2+}-sensitive dye. By dual-color imaging, receptor assembly and the cytosolic
156 calcium concentration were simultaneously recorded in living cells over the matrices. Upon
157 addition of *tris*$NTA^{PEG12-B}$, receptor recruitment led to a twofold increase in cytosolic calcium
158 concentration with a rapid rise within two minutes (Fig 3B, C), contrary to control matrices
159 without SA (Fig EV5). This indicates that calcium signals are associated with the motility
160 change. To correlate ligand-free *versus* canonical receptor activation, the agonist porcine
161 neuropeptide Y (pNPY, K_D = 5.2 ± 2.0 nM) was added to pre-patterned cells. An increase in
162 cytosolic Ca^{2+} was detected, which reached a plateau after one minute, followed by a slow
163 decay of the signal over a period of four minutes (Fig 3B, C). Strikingly, more receptors were
164 recruited to the patterned areas after activation via the agonist, as reflected by the increase in
165 integrated density in the patterned regions (Fig 3D). These results indicate that ligand-
166 activated Y_2Rs diffuse into areas where increased receptor density is present and
167 preferentially localized there. Recently, specific clusters termed GPCR hot spots (40-300 nm)
168 were visualized at the plasma membrane of living cells (Calebiro & Jobin, 2019; Chavez-
169 Abiega *et al.*, 2019; Hilger *et al.*, 2018; Sungkaworn *et al.*, 2017). These hot spots represent
170 regions where signaling preferentially occurs and where both receptors and G proteins are

171 enriched. We hypothesize that the induced microscale clusters may also trigger the formation
172 of hot spots providing the ideal environment for recruitment of more active receptors and thus
173 amplification of the signal. By increasing the local effective receptor concentration, this
174 complex organization may increase both the speed and efficiency of receptor-G protein
175 coupling while enabling local signaling transduction.
176
177 **Downstream signaling by ligand-free receptor clustering**
178 We next explored the impact of receptor clustering on downstream signaling. GPCR
179 desensitization involves a complex series of events, e.g. receptor phosphorylation, arrestin-
180 mediated internalization, receptor recycling, and lysosomal degradation (Ziffert et al, 2020).
181 Short-term desensitization occurs within minutes and is primarily associated with arrestin
182 preventing G protein interaction with the GPCR. Arrestins bind to activated, phosphorylated
183 GPCRs and block receptor-G protein interaction by steric hindrance at the receptor-coupling
184 interface, while serving as adaptors for key components of the endocytic machinery and
185 numerous signaling proteins (Hilger et al, 2018, Wang et al, 2020). In the presence of high
186 concentrations of the canonical ligand, an Arr3-dependent internalization, subsequent
187 endosomal sorting, and recycling of Y_2R to the cell membrane were observed (Walther *et al.*,
188 2010; Wanka *et al.*, 2018). However, recent studies demonstrated a strong and persistent
189 activation of the $G_{\alpha i}$-pathway upon Y_2R activation, which depletes the intracellular G protein
190 repertoire before Arr3 binding can terminate signaling (Ziffert et al, 2020). To assess whether
191 ligand-free clustering leads to Arr3 recruitment, we transfected cells stably expressing the Y_2R
192 with $Arr3^{mCherry}$ (in brief Arr3) and monitored Arr3 recruitment in real-time by total internal
193 reflection fluorescence (TIRF) microscopy (Fig 4A). Upon microscale receptor confinement by
194 *tris*$NTA^{PEG12-B}$, we did not observe a significant increase in Arr3 recruitment by intensity-
195 contrast analysis of the patterned spots, whereas a significant Arr3 recruitment was detected
196 upon addition of the agonist pNPY (Fig 4B, C). Again, an increase in Y_2R density in the
197 clustered areas was detected upon addition of pNPY (Fig 4B, D). In a subsequent step, a
198 partial dissipation of the Y_2R/Arr3 assemblies by specific competition with histidine was

observed (Fig 4B, C). Interestingly, half of the intensity in the patterned regions was dissipated in the presence of the pNPY, indicating that not all receptors within the cluster areas are associated with the nanotool upon addition of the ligand. In addition, patterning of Arr3 was also detected in cells on an anti-His_6 antibody matrix within the first minutes after addition of pNPY (Fig EV6). In this case, we did not observe a significant change in receptor density upon addition of the pNPY, indicating that the high degree of immobilization and large size of the antibody might restrict the transient enrichment of active receptors into the clustered regions. Overall, our results reflect a difference between Arr3 recruitment in the ligand-free mode compared to ligand-activated state. These observations indirectly confirm a high-affinity interaction between the Y_2R and $G\alpha_i$ (Ziffert et al, 2020) and suggest an active recruitment of G proteins that delay Arr3 recruitment and impair termination of G protein signaling.

Receptor diffusion and dynamic exchange in confined regions

GPCR signaling results from dynamic interactions among receptors, G proteins, and the complex surrounding membrane environment, which confers flexibility and versatility on this fundamental biological process. GPCR hot spots are highly heterogeneous in terms of diffusion of receptors and G proteins, which rapidly switch among phases of rapid and slow diffusion (Calebiro & Jobin, 2019; Sungkaworn *et al.*, 2017). First, we examined whether Y_2R clustering affects lipid diffusion and distribution by labeling the membrane with the lipid-like dye CellMask. We observed a homogeneous staining of the plasma membrane, demonstrating that receptor confinement does not affect membrane organization (Fig EV7). To determine diffusion coefficients (*D*), we performed fluorescence recovery after photobleaching (FRAP) technique. *In situ* receptor clustering was triggered on Y_2R-expressing cells cultured on SA-matrices by addition of *tris*$NTA^{PEG12\text{-}B}$ (100 nM, 10 min). In a subsequent step, the membrane was labeled and square-shaped regions of interest (ROIs) covering four 1 µm-sized spots were photobleached. Fluorescence recovery was analyzed by a FRAP simulation approach that enabled calculation of diffusion coefficients independent of bleaching geometry (Blumenthal *et al.*, 2015). The diffusion coefficient of lipids obtained by FRAP

227 showed an average value of D_{lipid} = 0.66 ± 0.10 μm^2/s in agreement with literature values for
228 free Brownian lipid diffusion at the plasma membrane (Schwille *et al.*, 1999; Wawrezinieck *et*
229 *al.*, 2005).

230 To evaluate the Y_2R mobility in the ligand-free induced clusters, we determined the receptor
231 lateral diffusion of Y_2R-expressing cells cultured on SA-matrices before and after addition of
232 trisNTA$^{PEG12-B}$ (100 nM, 10 min). A square-shaped ROI covering four 1 μm-sized spots and
233 recovery was photobleached. A significant decrease in the lateral diffusion of the Y_2R was
234 observed at the basal membrane of cells after receptor confinement by *tris*NTA$^{PEG12-B}$ (D_{before}
235 = 0.25 ± 0.08 μm^2/s *versus* D_{after} = 0.10 ± 0.03 μm^2/s) (Fig 5A, E). Surprisingly, the receptor
236 density showed a high recovery within ~3 min after photobleaching (Fig 5A, Fig EV8, Movie 2).
237 Notably, no significant difference in receptor mobile fraction (M_f) before and after addition of
238 the nanotool was observed (M_f = 0.80 ± 0.04) (Fig 5B). Importantly, FRAP analyses of cells
239 cultured on matrices functionalized with anti-His$_6$ antibodies presented a significant decrease
240 in the receptor diffusion as well as in the M_f at the clustered spots ($M_{f,anti\text{-}His6\ Ab}$ = 0.56 ± 0.08)
241 (Fig 5B, Fig EV9, Movie 3). In contrast to monovalent antibody immobilization, receptor
242 clustering by the multivalent interaction nanotool is dynamic, allowing fast exchange of His$_6$-
243 tagged receptors or competition by histidine. We rationalized that free receptors can diffuse
244 into the clustered spots and exchange with photobleached receptors at multivalent binding
245 sites, leading to a dynamic confinement. Our results point out that a high receptor exchange
246 is possible even in micrometer-sized clusters, an effect that likely depends on cluster size,
247 with larger clusters showing less recovery (Sánchez *et al.*, 2021).

248 Finally, we investigated the lateral receptor mobility with a higher spatiotemporal resolution
249 using imaging fluorescence correlation spectroscopy (imFCS). FCS is used to study the
250 diffusion of membrane proteins in living cells with single-molecule sensitivity (Fig 5C). These
251 multiplexed FCS measurements are realized by analyzing many pixels simultaneously using
252 a widefield setup (Harwardt et al, 2018, Kannan et al, 2006). Regions of interests (ROIs) on
253 Y_2R-expressing cells cultured on SA-matrices were analyzed before and after addition of
254 *tris*NTA$^{PEG12-B}$. Enrichment of Y_2R at the basal membrane was observed with total internal

255 reflection fluorescence (TIRF) microscopy (Fig 5D). Consistent with the FRAP measurements,
256 a decrease in the Y_2R diffusion coefficient was determined upon cluster formation (D_{before} =
257 0.32 ± 0.06 $\mu m^2/s$ and D_{after} = 0.16 ± 0.05 $\mu m^2/s$). The receptor diffusion coefficient measured
258 before clustering is comparable to similar membrane proteins (Lippincott-Schwartz et al,
259 2001), demonstrating that the microstructured confinement does not affect the mobile fraction
260 of receptors. In contrast to FRAP, imFCS provides a two-dimensional diffusion map, which
261 enables the determination of local differences in the lateral diffusion coefficient of membrane
262 receptors with high precision. Quantitative analysis of the 1 µm cluster spots in the acquired
263 ROIs resulted in a lateral diffusion coefficient of D_{spots} = 0.14 ± 0.03 $\mu m^2/s$ (Fig 5E). Taking into
264 consideration that imFCS detects only mobile particles, we determined a similar decrease in
265 lateral diffusion in the patterned regions (Fig EV9) for cells cultured on matrices functionalized
266 with anti-His_6 antibodies. Taken together, we unravel that in microscale clusters, associations
267 between His_6-tagged Y_2Rs and multivalent *tris*$NTA^{PEG12-B}$ resulted in decreased diffusion rate
268 but dynamic receptor exchange with unchanged mobile fraction, which is similar to the
269 behavior described upon ligand-activated receptor clustering. This plasticity of the confined
270 receptors likely has a relevant impact on the efficiency of hot spot formation and GPCR
271 signaling.
272

273 **Discussion**

274 We developed a versatile concept to cluster receptors *in situ* with minimal steric hindrance
275 and disturbance. Ligand-independent receptor activation by confinement was unraveled by
276 cytosolic calcium increase and changes in cell spreading and motility. Addition of the canonical
277 ligand led to a similar calcium increase and interestingly, an amplification of the signal was
278 observed in the clustered areas concomitant with an increased receptor density. Surprisingly,
279 we revealed a difference in triggering of downstream signaling for the ligand-free *versus*
280 ligand-activated receptors as evidenced by co-recruitment of Arr3 to the clustered spots only
281 occurring in the presence of the canonical ligand. These findings are consistent with previous
282 results demonstrating an Arr3-dependent internalization, subsequent endosomal sorting, and

283 receptor recycling to the cell membrane in the presence of high concentrations of NPY
284 (Walther *et al.*, 2010; Wanka *et al.*, 2018). We hypothesize that high-affinity $Y_2R/G\alpha_i$
285 interactions drive the initial cell response, cytosolic calcium increase, and cell motility. High
286 local receptor density in the spots increases the residence time of proximate $G\alpha_i$ proteins and
287 recruits further downstream effectors, which boost the probability of activation (Sánchez *et al.*,
288 2021). Further, $Y_2R/G\alpha_i$ interactions lead to persistent activation of the $G\alpha_i$ pathway, which
289 depletes the intracellular $G\alpha_i$ protein repertoire before Arr3 binding can terminate signaling
290 (Ziffert *et al.*, 2020). The time frame of imaging after addition of the nanotool (30 min) suggests
291 a long-lasting $G\alpha_i$ protein activation and favors the hypothesis of a mechanism for Y_2R
292 activation and desensitization that is limited to the cell membrane and partially independent of
293 Arr3 recruitment (Ziffert *et al.*, 2020).

294 Many transmembrane receptors form dynamic assemblies that promote downstream signal
295 transduction in cells. Recently, dynamic liquid-like microscale clusters were identified as
296 critical modulators of cell signaling (Case *et al.*, 2019; Lyon *et al.*, 2021). In our system, the
297 transient association between the nanotool and the receptors revealed the generation of a
298 dynamic platform for cell signaling, which may have characteristics akin liquid-like clusters
299 generated by LLPS. The dynamic exchange of molecules within induced Y_2R microscale
300 clusters may contribute to hot spots formation and final downstream signaling. This
301 characteristic together with the lower concentration required compared to established systems
302 with immobilized ligands or antibodies, highlight the relevance of this versatile approach along
303 with the developed nanotool. Multiscale analyses of the multivalent interactions between
304 receptor condensates, G proteins, the lipid environment and actin–myosin assemblies are
305 critical to confirm the cluster behavior and dynamics. *In vitro* reconstitution systems utilizing
306 lipid bilayers have proven phase-segregation in two dimensions (Banjade & Rosen, 2014;
307 Ditlev *et al.*, 2019). The comparison of a mobile system based on model membranes and our
308 established platform, together with advanced quantitative fluorescence microscopy
309 techniques such as fluorescence resonance energy transfer (FRET) and single-molecule
310 localization microscopy will help us to decode condensates behavior and ligand-independent

311 signaling. In summary, the developed tool and matrices allow the investigation of ligand-
312 independent receptor activation *in situ* facilitating the investigation of early key processes in
313 cell signaling.

314 **Materials and Methods**

315 **Synthesis of *tris*NTA$^{PEG12-B}$:** Cyclam-Lys-*tris*NTA (Gatterdam *et al.*, 2018) (5.0 mg, 4.8 µmol),
316 Biotin-PEG$_{12}$-NHS (23.0 mg, 24.0 µmol) and DIPEA (12.2 µL, 72.0 µmol) were dissolved in
317 0.5 ml dry DMF and stirred for 2 h at RT. After reaction, the volatile components were removed
318 by lyophilization. Raw product was purified by semi-preparative RP-HPLC (mobile phase A:
319 H_2O + 0.1% TFA, B: CAN + 0.1% TFA; gradient 5% to 80% B in 20 min; MZ-PerfectSil, 300
320 ODS, 5 µm, 250 x 10 mm, flow 4 ml/min). A biotin moiety was integrated into the nanotool for
321 immobilization to SA in the prestructured matrices. The PEG$_{12}$ linker between the biotin and
322 the *tris*NTA unit increased the flexibility of the molecule. *tris*NTA$^{PEG12-B}$ was confirmed by liquid
323 chromatography-mass spectrometry (LC-MS, Waters BioAccord System). Dataset was
324 recorded with an ACQUITY UPLC I-Class Plus chromatography system and ACQUITY RDa
325 Detector, which was set to a cone voltage of 25 V, capillary voltage of 1.2 kV and a desolvation
326 temperature of 500 °C operating in positive ionization mode. For reverse-phase separation,
327 an ACQUITY UPLC Peptide BEH C18 column (300 Å, 1.7 µm, 2.1 mm x 100 mm) was used
328 (Fig EV10). The *tris*NTA chelator compounds were dissolved in HBS buffer (20 mM HEPES-
329 NaOH pH 7.5, 150 mM NaCl) and incubated with tenfold excess of $NiCl_2$. After 30 min
330 incubation at 4 °C, the excess of Ni(II) was separated by ultra-centrifugal filters (Amicon Ultra-
331 0.5 ml; 3 kDa and 10 kDa MWCO).

332

333 **Microcontact printing.** Large-area microcontact printing was performed as described
334 previously (Lanzerstorfer *et al.*, 2020) with modifications. In short, a field of a large-area PFPE
335 elastomeric stamp (1 µm grid size), obtained by the EV-Group (St. Florian am Inn, Upper
336 Austria, Austria), was cut out, and washed by flushing with ethanol (100%) and distilled water.
337 After drying with nitrogen, the stamp was incubated in 50 ml BSA solution (1 mg/ml, Sigma-
338 Aldrich) for 30 min followed by washing the stamp with phosphate-buffered saline (PBS) and
339 distilled water. After drying with nitrogen, the stamp was placed with homogeneous pressure
340 onto a clean epoxy-coated glass substrate (Schott Nexterion Slide E) and incubated overnight

341 at 4 °C. The next day, the stamp was stripped from the glass with a forceps, and the
342 microstructured glass was bonded to a 96-well plastic casting using an adhesive tape (3M)
343 and closed with an appropriate lid.
344
345 **Functionalization of the prestructured matrices.** BSA-prestructured wells were incubated
346 with biotin-BSA (0.1 mg/ml, Thermo Fisher Scientific) and SA (1 µM, Sigma-Aldrich) in PBS,
347 each for 1 h at RT. Incubated wells were washed thoroughly with PBS after each step, to
348 remove unbound biotin-BSA and SA. For binding of soluble His-tagged proteins, wells were
349 incubated with *tris*NTA$^{PEG12-B}$ (0.5 µM) in HBS buffer for 1 h at RT. For nickel-loading, the
350 prestructured matrices were sequentially incubated with imidazole (1 M, 2 min), EDTA
351 (100 mM, 2 min), and $NiCl_2$ (10 mM, 5 min). Wells were carefully washed after each step.
352 Finally, HBS buffer containing EDTA (50 µM) was used to remove the free, non-complexed
353 nickel ions. His_6-GFP (100 nM) previously expressed and purified was added to the wells and
354 incubated for 30 min at RT. Experiments were performed in biological replicas (N=5).
355
356 **Cell culture.** HeLa Flp-In™ T-Rex™ Y_2R cells (His_6-Y_2R^{mEGFP} or Y_2R^{mEGFP}) were generated as
357 previously described (Sánchez *et al.*, 2021) and cultured at 37 °C, 5% CO_2, and 95% humidity.
358 For culturing the stable cell line, high glucose Dulbecco's modified Eagle's medium (DMEM)
359 (Gibco/Thermo Fisher Scientific) was supplemented with 10% tetracycline-free fetal calf
360 serum (FCS, Bio&Sell), blasticidin S HCl (1 µg/ml, Thermo Fisher Scientific) and
361 hygromycin B (50 µg/ml, Thermo Fisher Scientific). To induce receptor expression, the cell
362 medium was replaced with fresh medium containing tetracycline (0.1 µg/ml, Fluka) 18 h before
363 imaging. The same concentration of tetracycline resulting in an efficient plasma membrane
364 targeting was used for all the experiments. The cells were regularly tested for mycoplasma
365 contamination.
366

367 **Receptor confinement in *real-time* by *tris*NTA$^{PEG12-B}$.** Cells expressing Y_2R (His_6-Y_2R^{mEGFP}
368 or Y_2R^{mEGFP}) were trypsinized and allowed to adhere to SA prestructured matrices for 3 h or
369 overnight. 15-18 h prior to the experiment, the cell medium was replaced with fresh medium
370 containing tetracycline (0.1 µg/ml) to induce receptor expression. The cells were visualized by
371 CLSM in live-cell imaging solution (LCIS, Thermo Fisher Scientific) at 37 °C. Cells were
372 subsequently incubated with nickel-loaded *tris*NTA$^{PEG12-B}$ (100 nM) in LCIS for 10-15 min at
373 37 °C. Excess of unbound *tris*NTA$^{PEG12-B}$ was removed by washing with LCIS. For reversibility
374 experiments, micropatterned cells were incubated with histidine (5 mM) in LCIS for 2 to 10 min
375 followed by washing with LCIS. Experiments were performed in biological replicas (N=4).
376
377 **Receptor confinement on antibody-micropatterned matrices.** Wells prestructured with
378 BSA were subsequently incubated with biotin-BSA (0.1 mg/ml), SA (1 µM), and a biotinylated
379 anti-His_6 antibody (1 µM) (ab106261, Abcam) in PBS for 1 h at RT. Wells were washed
380 thoroughly with PBS to remove unbound antibody. Cells expressing Y_2R were trypsinized and
381 seeded onto the antibody patterns. After 3 h, cells were visualized by CLSM in LCIS at 37 °C.
382 Experiments were performed in biological replicas (N=5).
383
384 **Time-lapse calcium imaging.** 18 h after seeding the cells onto prestructured SA-matrices,
385 cells were incubated with BioTracker 609 Red Ca^{2+} AM dye (3 µM, Merck Millipore) in fresh
386 medium for 30 min. The cell-membrane permeable dye is de-esterified by cellular esterases
387 and remains trapped in the cytosol. After incubation with the Ca^{2+} dye, cells were rinsed three
388 times with PBS and imaged by CLSM in LCIS at 37 °C. For investigation of Ca^{2+} signal, time-
389 lapse images were taken (5 slices z-stacks, 45-s interval) before and after addition of
390 *tris*NTA$^{PEG12-B}$. Fluorescence intensity (($\lambda_{ex/em}$ 590/609 nm) of the dye changes depending on
391 the intracellular Ca^{2+} concentration. Maximum intensity projections of single channels were
392 analyzed. The ImageJ ROI tool was used to define the areas of the image to be analyzed. We
393 consider a ROI covering the complete cell contour. Mean gray value (F) were background

394 subtracted and normalized to the fluorescence in cells before F_0. Experiments were performed
395 in biological replicas (N=3).
396
397 **Plasma membrane staining.** Live-cell membrane staining was performed directly after
398 receptor assembly in living cells grown on prestructured matrices. CellMask^{TM} deep red
399 plasma membrane stain (Thermo Fisher Scientific) was used according to manufacturer's
400 instruction. 1 µl of the stock solution (1000x dilution) was dissolved in 1 ml of warm LCIS (final
401 concentration 5 µg/ml) and subsequently added to the cells, incubated for 5 min at 37 °C, and
402 washed with LCIS before visualization. Experiments were performed in biological replicas
403 (N=3).
404
405 **Confocal laser scanning microscopy.** Images were recorded by using a CLSM Zeiss LSM
406 880 (Carl Zeiss) equipped with a Plan-Apochromat 63x/1.4 Oil DIC M-27 objective. Sequential
407 settings for dual-color imaging were used. Excitation wavelengths for the different
408 fluorophores: 488 nm (argon laser) for mEGFP; 594 nm for the Ca^{2+} dye; 633 nm (helium-
409 neon laser) for the plasma membrane dye. Signals were detected after appropriate filtering on
410 a photomultiplier. Intensities of channels were adjusted over the whole image for better
411 visualization of overlap and exported by Zen blue (version 2.3 lite, Zeiss). Detector
412 amplification, laser power, and pinhole were kept constant for all studies.
413
414 **Image analysis.** Fluorescence images were processed with Zen blue, ImageJ, and Fiji
415 software (Schindelin *et al.*, 2012; Schneider *et al.*, 2012). All images were background
416 subtracted. Integrated density, mean gray value and cell area were obtained with ImageJ.
417 Graphs were plotted with OriginPro.
418

419 **Fluorescence recovery after photobleaching.** FRAP experiments were conducted at the
420 CLSM Zeiss LSM 880 using 63 x/1.4 Oil DIC objective. Rectangular-shaped regions (6-10 μm
421 radius) were bleached within 10 s with high laser intensities. Fluorescence recovery was
422 monitored by repetitively imaging an area containing the photobleached region at 0.1 frame/s
423 for ~ 150 s. For the analysis, a simulation approach that allows computation of diffusion
424 coefficients regardless of bleaching geometry used in the FRAP series was applied
425 (Blumenthal *et al.*, 2015). The method is based on fitting a computer-simulated recovery to
426 actual recovery data of a FRAP series. The algorithm accepts a multiple-frame TIFF file,
427 representing the experiment as input, and simulates the (pure) diffusion of the fluorescent
428 probes (*2D* random walk) starting with the first post-bleach frame of the actual data. Once the
429 simulated recovery is finished, the algorithm fits the simulated data to the real one and extracts
430 the diffusion coefficient. The algorithm iteratively creates a series of simulated images, where
431 each frame corresponds to a single iteration. The intensity values are extracted from the (user
432 indicated) bleached area of the simulated frames, thus determining the general shape of the
433 recovery curve. The "time" axis at this stage is in arbitrary units (iterations). To extract the
434 diffusion coefficient, the simulated recovery curve needs to be fitted to the real recovery curve,
435 by appropriately stretching the "time" axis. The time between frames in the actual data set is
436 obviously known, thus once overlapping optimally the simulated curve with the real one, the
437 duration of one iteration, in *real-time* units, is determined. The diffusion coefficient of the
438 simulated series is then calculated according to eq. 1,
439 where D_s is the simulation-extracted diffusion coefficient, l is the step of a molecule in each

$$D_s = \frac{l^2}{4t_i} \tag{1}$$

440 iteration of the simulation, corresponding to one pixel in the image (the pixel size is calibrated
441 previously, by imaging a known calibration sample), and t_i is the time interval between steps
442 (determined as explained). Technically, the simulation proceeds until a plateau is reached
443 (equilibration of the fluorescence intensity in the bleached area). The number of data points in
444 the simulated recovery is typically different (larger) than the number of experimental points. In

445 addition, the real experimental data may not have been acquired until equilibration of
446 fluorescence. To determine t_i, the algorithm scans a range of possible values for the total
447 duration represented by the simulation and calculates a value X^2 for the goodness-of-fit
448 between the simulated data and the real FRAP data. Total simulation duration is selected as
449 the one that produces the minimal X^2. Experiments were performed in biological replicas
450 (N=3).
451
452 **imFCS measurements**. imFCS measurements were performed as described earlier
453 (Harwardt *et al.*, 2018; Harwardt *et al.*, 2017). A home-built widefield setup with total internal
454 reflection fluorescence (TIRF) illumination was used for imFCS analysis. The experimental
455 setup was equipped with a 488 nm diode laser (100 mW, Obis, Coherent, USA). The excitation
456 light passes through an acousto-optical tunable filter (AA Opto-Electronic, Orsay, France) and
457 a telescope consisting of two achromatic lenses (Thorlabs, USA) with f = -40 mm and 750 mm.
458 A third achromatic lens (f = 400 mm, Thorlabs) directed the excitation light to the TIRF mirror
459 and had its focus on the back focal plane of the objective. The TIRF mirror was placed on a
460 motorized translation stage (25 mm, #MTS25/M-Z8, Thorlabs) controlled by a motion
461 controller (K-Cube Brushed DC Servo Motor Controller, # KDC101, Thorlabs) to switch
462 between widefield and TIRF illumination. The light entered an Eclipse Ti microscope (Nikon,
463 Japan), was reflected by a dichroic mirror (TIRF-Quad filter set 405/488/561/640 consisting of
464 a QuadLine Laser Clean-up ZET405/488/561/640x, QuadLine dichroic zt405/488/561/640rpc,
465 QuadLine rejection band ZET405/488/561/640 TIRF, all AHF Analysentechnik AG, Tübingen,
466 Germany), and was directed by an oil-immersion TIRF objective (UapoN 100xOTIRF, 1.49
467 Oil, Olympus, Japan) onto the sample. A nosepiece stage (IX2-NPS, Olympus) was used for
468 z plane adjustment and drift minimization. Emission light was collected by the same objective
469 and passed the dichroic mirror. In the detection path a TwinCam (Acal Bfi, Germany) with a
470 BrightLine HC 525/45 bandpass filter (AHF Analysentechnik AG) was implemented and the
471 signal was detected by a scientific complementary metal-oxide semiconductor (sCMOS)
472 camera (Zyla 4.2, Andor, Belfast, UK). Data were collected using the open-source software

473 μManager (Edelstein *et al.*, 2010). For data acquisition the following settings were applied:
474 24 W/cm^2 laser intensity, a bit depth of 16 bit, pixel readout rate of 540 MHz, frame time 4 ms,
475 4x4 binning, and 4,000 frames per film. For each film, a 40x25 pixel (or 40x20 pixel) region of
476 interest (ROI) was chosen and the measurement was performed with TIRF illumination to
477 observe membrane diffusion of Y_2R. In total 36 untreated cells, 24 cells with *tris*NTA$^{PEG12-B}$
478 immobilized receptors, and 26 cells with anti-His$_6$ antibody immobilized receptors were
479 measured. Each condition contains data from at least three independent measurement days
480 (N=3).
481
482 **imFCS data analysis**. Analysis of imFCS films was performed using the imFCS plugin
483 (version 1.52) (Sankaran *et al.*, 2010) for Fiji (Schindelin *et al.*, 2012). The following correlation
484 settings were chosen: emission wavelength = 515 nm, NA = 1.49, correlator scheme P = 16
485 and Q = 8, lateral PSF = 0.8, binning = 1, pixel size = 5.75 μm, magnification = 25 for 4x4
486 binning, and linear segment bleach correction with linear segments of 500 frames. Diffusion
487 coefficients were obtained for each pixel by fitting the correlation curves according to the
488 literature (Sankaran *et al.*, 2010). To compare the overall diffusion coefficients with those of
489 the patterned regions, ROIs were placed around patterned regions and analyzed separately.
490 For further analysis, the pixelwise diffusion coefficients for all measurements were imported
491 into OriginPro 2019 (OriginLab Corporation, Northampton, USA). For box plots of diffusion
492 coefficients, median diffusion coefficients were determined for each cell. Mean diffusion
493 coefficients per condition were obtained by averaging over the median diffusion coefficients
494 per measurement and calculating the standard error of the mean. Two-sample t-tests (α =
495 0.05) were applied to compare the diffusion coefficients for the different conditions. All
496 datasets were tested for normality using the Kolmogorov-Smirnov test (α = 0.05). Significance
497 was assigned as follows: $p > 0.05$ no significant difference between populations (n.s.), $p <$
498 0.05 significant difference (*), $p < 0.01$ significant difference (**), and $p < 0.001$ significant
499 difference (***). Two-dimensional maps of diffusion coefficients were generated also in
500 OriginPro. Diffusion coefficients were color coded from light yellow to dark red in the range of

501 0 to 0.5 µm²/s. Pixels that yielded correlation curves with diffusion coefficients higher than
502 0.5 µm²/s are presented in black. Pixels that yielded correlation curves which could not be
503 fitted by the imFCS plugin in Fiji are shown in light grey. To generate frequency distribution
504 plots, diffusion coefficients were log-transformed and binned in the interval between -5.3 and
505 1.0 with a bin size of 0.1 for each cell. Logarithmic diffusion coefficients were re-transformed,
506 frequency counts were averaged over all cells per condition and normalized. Frequency
507 counts were plotted logarithmically against diffusion coefficients. Errors bars represent
508 standard errors of the mean.
509
510 **Arr3 recruitment upon receptor confinement**. Microstructured surfaces were functionalized
511 with biotin-BSA and SA or SA and anti-His_6 antibody as described before. For transient co-
512 transfection with $Arr3^{mCherry}$, cells were sub-cultured the day before and then transfected with
513 the $Arr3^{mCherry}$ plasmid using the TurboFect™ transfection reagent (Thermo Fisher Scientific,
514 Waltham, MA, USA), according to the manufacturer's instructions and induced with
515 Tetracycline (0.1 µg/ml) 18 h before microscopy. Cells co-expressing His_6-Y_2R^{mGFP} and Arr3
516 were seeded onto the microstructured matrices and visualized by total internal reflection
517 fluorescence (TIRF) microscopy in LCIS at 37 °C after 3 to 4 h to ensure a homogeneous cell
518 membrane adhesion, which is a prerequisite for quantitative TIRF microscopy. For antibody
519 experiments, cells grown on prestructured matrices were incubated with pNPY (10 nM, Tocris)
520 in LCIS for 30 min at 37 °C. For *tris*$NTA^{PEG12-B}$ experiments, cells grown on SA-matrices were
521 subsequently incubated with nickel-loaded *tris*$NTA^{PEG12-B}$ (100 nM) and pNPY (10 nM) in LCIS
522 for 30 min at 37 °C. For reversibility, cells were incubated with histidine (5 mM) in LCIS for
523 30 min. Experiments were performed in biological replicas (N=2).
524
525 **Arr3 imaging by TIRF microscopy**. The detection system was set up on an epi-fluorescence
526 microscope (Nikon Eclipse Ti2). For selective fluorescence excitation of mGFP and mCherry,
527 a multi-laser engine (Toptica Photonics, Munich, Germany) was used at 488 and 561 nm,
528 respectively. The samples were illuminated in total internal reflection (TIR) configuration

529 (Nikon Ti-LAPP) using a 60x oil immersion objective (NA = 1.49, APON 60XO TIRF). After
530 appropriate filtering using standard filter sets, the fluorescence was imaged onto a sCMOS
531 camera (Zyla 4.2, Andor, Northern Ireland). The samples were mounted on an x-y-stage
532 (CMR-STG-MHIX2-motorized table, Märzhäuser, Germany), and scanning was supported by
533 a laser-guided automated Perfect Focus System (Nikon PFS).
534
535 **Contrast Quantification and Statistical Analysis**. Contrast analysis was performed as
536 described previously (Lanzerstorfer *et al.*, 2014; Lanzerstorfer *et al.*, 2020; Schütz *et al.*,
537 2017). Initial imaging recording was supported by the Nikon NIS Elements software. Images
538 were exported as TIFF frames and fluorescence contrast analysis was performed using the
539 Spotty framework (Borgmann *et al.*, 2012). The fluorescence contrast <c> was calculated as
540 $\langle c \rangle = (F^{+} - F^{-})/(F^{+} - F_{bg})$, where F^{+} denotes the intensity of the inner pixels of the pattern. F^{-}
541 shows the intensity of the surrounding pixels of the micropattern, and F_{bg} the intensity of the
542 global background. Data are expressed as the means ± SEM. Comparisons of more than two
543 different groups were performed using one-way ANOVA, which was followed by Tukey's
544 multiple comparisons test in GraphPad Prism software (version 9.1.2).

545 **Acknowledgements**

546 We thank Christian Winter, Andrea Pott, Inga Nold, and all members of the Institute of
547 Biochemistry (Goethe University Frankfurt) for discussion and comments. We thank Dr.
548 Annette Beck-Sickinger (Leipzig University) for the Y_2 receptor construct and Dr. Alina Klein
549 (Goethe University Frankfurt) for the generation of the Y_2R^{mEGFP} constructs with and without
550 His_6-tag. We tank Dr. Cornelius Krasel (Philipps University of Marburg) for the $Arr3^{mCherry}$
551 construct. We also thank Christian Winter for the LC-MS analysis. This work was supported
552 by the German Research Foundation (GRK 1986 (No. 237922874) to R.W. and R.T.; CRC
553 807 (No. 57566863) P16 to R.T.), LOEWE DynaMem P3 to R.W. and R.T., the Volkswagen
554 Foundation (Az. 96 498 to R.W., Az. 96 497 to M.H., and Az. 96 496 to R.T.); the Christian-
555 Doppler Forschungsgesellschaft (Josef Ressel Centre for Phytogenic Drug Research, the
556 Austrian Science Fund (FWF, I4972-B) and the FH Upper Austria Center of Excellence for
557 Technological Innovation in Medicine (TIMed Center) to U.M., J.W. and P.L..

558

559 **Author contributions**

560 M.F.S. performed the cell-based assays and imaging experiments. M.S.D. carried out the
561 imFCS experiments and analyzed the data together with M.H.. U.M., P.L., and J.W. prepared
562 the prestructured surfaces, performed the Arr3 recruitment assays and the intensity-contrast
563 analysis. K.G. synthesized and characterized the chelator compound. M.F.S., R.W., and R.T.
564 wrote the manuscript with contributions from all authors. R.T. conceived the study.

565

566 **Competing interest.** The authors declare no competing interest.

567

568 **Data availability.** Data and movies are available in the supplementary materials.

569 **References**

570 Bag N, Huang S, Wohland T (2015) Plasma Membrane Organization of Epidermal Growth
571 Factor Receptor in Resting and Ligand-Bound States. *Biophys J* **109:** 1925-36.
572 Banjade S, Rosen MK (2014) Phase transitions of multivalent proteins can promote
573 clustering of membrane receptors. *Elife* **3**
574 Bernard A, Renault JP, Michel B, Bosshard HR, Delamarche E (2000) Microcontact printing
575 of proteins. *Advanced Materials* **12:** 1067-70.
576 Blumenthal D, Goldstien L, Edidin M, Gheber LA (2015) Universal Approach to FRAP
577 Analysis of Arbitrary Bleaching Patterns. *Sci Rep* **5:** 11655.
578 Boncompain G, Herit F, Tessier S, Lescure A, Del Nery E, Gestraud P, Staropoli I, Fukata Y,
579 Fukata M, Brelot A, Niedergang F, Perez F (2019) Targeting CCR5 trafficking to inhibit
580 HIV-1 infection. *Sci Adv* **5:** eaax0821.
581 Borgmann D, Weghuber J, Schaller S, Jacak J, Winkler SM (2012) Identification of patterns
582 in microscopy images of biological samples using evolution strategies. In *Proceedings*
583 *of the 24th European Modeling and Simulation Symposium*.
584 Calebiro D, Jobin ML (2019) Hot spots for GPCR signaling: lessons from single-molecule
585 microscopy. *Curr Opin Cell Biol* **57:** 57-63.
586 Case LB, Ditlev JA, Rosen MK (2019) Regulation of Transmembrane Signaling by Phase
587 Separation. *Annu Rev Biophys* **48:** 465-94.
588 Chavez-Abiega S, Goedhart J, Bruggeman FJ (2019) Physical biology of GPCR signalling
589 dynamics inferred from fluorescence spectroscopy and imaging. *Curr Opin Struct Biol*
590 **55:** 204-11.
591 Chen Y, Munteanu AC, Huang YF, Phillips J, Zhu Z, Mavros M, Tan W (2009) Mapping
592 receptor density on live cells by using fluorescence correlation spectroscopy. *Chemistry*
593 **15:** 5327-36.
594 Ditlev JA, Vega AR, Koster DV, Su X, Tani T, Lakoduk AM, Vale RD, Mayor S, Jaqaman K,
595 Rosen MK (2019) A composition-dependent molecular clutch between T cell signaling
596 condensates and actin. *Elife* **8**
597 Doh J, Irvine DJ (2006) Immunological synapse arrays: patterned protein surfaces that
598 modulate immunological synapse structure formation in T cells. *Proc Natl Acad Sci U S*
599 *A* **103:** 5700-5.
600 Edelstein A, Amodaj N, Hoover K, Vale R, Stuurman N (2010) Computer control of
601 microscopes using μManager. *Curr Protoc Mol Biol* **Chapter 14:** Unit14.20.
602 Ekstrand AJ, Cao R, Bjorndahl M, Nystrom S, Jonsson-Rylander AC, Hassani H, Hallberg B,
603 Nordlander M, Cao Y (2003) Deletion of neuropeptide Y (NPY) 2 receptor in mice
604 results in blockage of NPY-induced angiogenesis and delayed wound healing. *Proc Natl*
605 *Acad Sci U S A* **100:** 6033-8.

606 Gatterdam K, Joest EF, Gatterdam V, Tampe R (2018) The scaffold design of trivalent
607 chelator heads dictates affinity and stability for labeling His-tagged proteins in vitro and
608 in cells. *Angew Chem Int Ed Engl* **57:** 12395-9.
609 Hager R, Müller U, Ollinger N, Weghuber J, Lanzerstorfer P (2021) Subcellular Dynamic
610 Immunopatterning of Cytosolic Protein Complexes on Microstructured Polymer
611 Substrates. *ACS Sens*
612 Haqshenas G, Doerig C (2019) Targeting of host cell receptor tyrosine kinases by
613 intracellular pathogens. *Sci Signal* **12**
614 Harwardt MIE, Dietz MS, Heilemann M, Wohland T (2018) SPT and Imaging FCS Provide
615 Complementary Information on the Dynamics of Plasma Membrane Molecules. *Biophys*
616 *J* **114:** 2432-43.
617 Harwardt MIE, Young P, Bleymüller WM, Meyer T, Karathanasis C, Niemann HH, Heilemann
618 M, Dietz MS (2017) Membrane dynamics of resting and internalin B-bound MET
619 receptor tyrosine kinase studied by single-molecule tracking. *FEBS Open Bio* **7:** 1422-
620 40.
621 Hilger D, Masureel M, Kobilka BK (2018) Structure and dynamics of GPCR signaling
622 complexes. *Nat Struct Mol Biol* **25:** 4-12.
623 Huang L, Tan HY, Fogarty MJ, Andrews ZB, Veldhuis JD, Herzog H, Steyn FJ, Chen C
624 (2014) Actions of NPY, and its Y1 and Y2 receptors on pulsatile growth hormone
625 secretion during the fed and fasted state. *J Neurosci* **34:** 16309-19.
626 Kawai T, Akira S (2005) Pathogen recognition with Toll-like receptors. *Curr Opin Immunol*
627 **17:** 338-44.
628 Kupperman E, An S, Osborne N, Waldron S, Stainier DY (2000) A sphingosine-1-phosphate
629 receptor regulates cell migration during vertebrate heart development. *Nature* **406:** 192-
630 5.
631 Lafferty RA, Flatt PR, Irwin N (2021) Established and emerging roles peptide YY (PYY) and
632 exploitation in obesity-diabetes. *Curr Opin Endocrinol Diabetes Obes* **28:** 253-61.
633 Lanzerstorfer P, Borgmann D, Schütz G, Winkler SM, Höglinger O, Weghuber J (2014)
634 Quantification and kinetic analysis of Grb2-EGFR interaction on micro-patterned
635 surfaces for the characterization of EGFR-modulating substances. *PLoS One* **9:**
636 e92151.
637 Lanzerstorfer P, Müller U, Gordiyenko K, Weghuber J, Niemeyer CM (2020) Highly Modular
638 Protein Micropatterning Sheds Light on the Role of Clathrin-Mediated Endocytosis for
639 the Quantitative Analysis of Protein-Protein Interactions in Live Cells. *Biomolecules* **10:**
640 540.
641 Li MO, Rudensky AY (2016) T cell receptor signalling in the control of regulatory T cell
642 differentiation and function. *Nat Rev Immunol* **16:** 220-33.

643 Lindner D, Walther C, Tennemann A, Beck-Sickinger AG (2009) Functional role of the
644 extracellular N-terminal domain of neuropeptide Y subfamily receptors in membrane
645 integration and agonist-stimulated internalization. *Cell Signal* **21:** 61-8.
646 Luther SA, Cyster JG (2001) Chemokines as regulators of T cell differentiation. *Nat Immunol*
647 **2:** 102-7.
648 Lyon AS, Peeples WB, Rosen MK (2021) A framework for understanding the functions of
649 biomolecular condensates across scales. *Nat Rev Mol Cell Biol* **22:** 215-35.
650 Manz BN, Groves JT (2010) Spatial organization and signal transduction at intercellular
651 junctions. *Nat Rev Mol Cell Biol* **11:** 342-52.
652 Méndez-Couz M, Manahan-Vaughan D, Silva AP, González-Pardo H, Arias JL, Conejo NM
653 (2021) Metaplastic contribution of neuropeptide Y receptors to spatial memory
654 acquisition. *Behav Brain Res* **396:** 112864.
655 Mossman KD, Campi G, Groves JT, Dustin ML (2005) Altered TCR signaling from
656 geometrically repatterned immunological synapses. *Science* **310:** 1191-3.
657 Movafagh S, Hobson JP, Spiegel S, Kleinman HK, Zukowska Z (2006) Neuropeptide Y
658 induces migration, proliferation, and tube formation of endothelial cells bimodally via Y1,
659 Y2, and Y5 receptors. *Faseb j* **20:** 1924-6.
660 Nair PM, Salaita K, Petit RS, Groves JT (2011) Using patterned supported lipid membranes
661 to investigate the role of receptor organization in intercellular signaling. *Nat Protoc* **6:**
662 523-39.
663 Ojosnegros S, Cutrale F, Rodríguez D, Otterstrom JJ, Chiu CL, Hortigüela V, Tarantino C,
664 Seriola A, Mieruszynski S, Martínez E, Lakadamyali M, Raya A, Fraser SE (2017) Eph-
665 ephrin signaling modulated by polymerization and condensation of receptors. *Proc Natl*
666 *Acad Sci U S A* **114:** 13188-93.
667 Parker SL, Balasubramaniam A (2008) Neuropeptide Y Y2 receptor in health and disease.
668 *Br J Pharmacol* **153:** 420-31.
669 Pasquale EB (2010) Eph receptors and ephrins in cancer: bidirectional signalling and
670 beyond. *Nat Rev Cancer* **10:** 165-80.
671 Pike R, Ortiz-Zapater E, Lumicisi B, Santis G, Parsons M (2018) KIF22 coordinates CAR
672 and EGFR dynamics to promote cancer cell proliferation. *Sci Signal* **11**
673 Rosenbaum DM, Rasmussen SG, Kobilka BK (2009) The structure and function of G-
674 protein-coupled receptors. *Nature* **459:** 356-63.
675 Sánchez MF, Els-Heindl S, Beck-Sickinger AG, Wieneke R, Tampé R (2021) Photoinduced
676 receptor confinement drives ligand-independent GPCR signaling. *Science* **371**
677 Sánchez MF, Murad F, Gülcüler Balta GS, Martin-Villalba A, García-Sáez AJ, Carrer DC
678 (2018) Early activation of CD95 is limited and localized to the cytotoxic synapse. *Febs j*
679 **285:** 2813-27.

680 Sankaran J, Shi X, Ho LY, Stelzer EH, Wohland T (2010) ImFCS: a software for imaging
681 FCS data analysis and visualization. *Opt Express* **18:** 25468-81.
682 Schindelin J, Arganda-Carreras I, Frise E, Kaynig V, Longair M, Pietzsch T, Preibisch S,
683 Rueden C, Saalfeld S, Schmid B, Tinevez JY, White DJ, Hartenstein V, Eliceiri K,
684 Tomancak P, Cardona A (2012) Fiji: an open-source platform for biological-image
685 analysis. *Nat Methods* **9:** 676-82.
686 Schneider CA, Rasband WS, Eliceiri KW (2012) NIH Image to ImageJ: 25 years of image
687 analysis. *Nat Methods* **9:** 671-5.
688 Schütz GJ, Weghuber J, Lanzerstorfer P, Sevcsik E (2017) Protein Micropatterning Assay:
689 Quantitative Analysis of Protein-Protein Interactions. *Methods Mol Biol* **1550:** 261-70.
690 Schwille P, Korlach J, Webb WW (1999) Fluorescence correlation spectroscopy with single-
691 molecule sensitivity on cell and model membranes. *Cytometry* **36:** 176-82.
692 Scott FL, Stec B, Pop C, Dobaczewska MK, Lee JJ, Monosov E, Robinson H, Salvesen GS,
693 Schwarzenbacher R, Riedl SJ (2009) The Fas-FADD death domain complex structure
694 unravels signalling by receptor clustering. *Nature* **457:** 1019-22.
695 Sebestyen Z, Prinz I, Déchanet-Merville J, Silva-Santos B, Kuball J (2020) Translating
696 gammadelta (γδ) T cells and their receptors into cancer cell therapies. *Nat Rev Drug*
697 *Discov* **19:** 169-84.
698 Stallaert W, Brüggemann Y, Sabet O, Baak L, Gattiglio M, Bastiaens PIH (2018) Contact
699 inhibitory Eph signaling suppresses EGF-promoted cell migration by decoupling EGFR
700 activity from vesicular recycling. *Sci Signal* **11**
701 Su X, Ditlev JA, Hui E, Xing W, Banjade S, Okrut J, King DS, Taunton J, Rosen MK, Vale
702 RD (2016) Phase separation of signaling molecules promotes T cell receptor signal
703 transduction. *Science* **352:** 595-9.
704 Sungkaworn T, Jobin ML, Burnecki K, Weron A, Lohse MJ, Calebiro D (2017) Single-
705 molecule imaging reveals receptor-G protein interactions at cell surface hot spots.
706 *Nature* **550:** 543-7.
707 Tang T, Hartig C, Chen Q, Zhao W, Kaiser A, Zhang X, Zhang H, Qu H, Yi C, Ma L, Han S,
708 Zhao Q, Beck-Sickinger AG, Wu B (2021) Structural basis for ligand recognition of the
709 neuropeptide Y Y(2) receptor. *Nat Commun* **12:** 737.
710 Torres AJ, Wu M, Holowka D, Baird B (2008) Nanobiotechnology and cell biology: micro-
711 and nanofabricated surfaces to investigate receptor-mediated signaling. *Annu Rev*
712 *Biophys* **37:** 265-88.
713 Traub MC, Longsine W, Truskett VN (2016) Advances in Nanoimprint Lithography. *Annu*
714 *Rev Chem Biomol Eng* **7:** 583-604.
715 Tsukiyama T, Zou J, Kim J, Ogamino S, Shino Y, Masuda T, Merenda A, Matsumoto M,
716 Fujioka Y, Hirose T, Terai S, Takahashi H, Ishitani T, Nakayama KI, Ohba Y, Koo BK,

717 Hatakeyama S (2020) A phospho-switch controls RNF43-mediated degradation of Wnt
718 receptors to suppress tumorigenesis. *Nat Commun* **11:** 4586.
719 Venkatakrishnan AJ, Deupi X, Lebon G, Tate CG, Schertler GF, Babu MM (2013) Molecular
720 signatures of G-protein-coupled receptors. *Nature* **494:** 185-94.
721 Walther C, Nagel S, Gimenez LE, Mörl K, Gurevich VV, Beck-Sickinger AG (2010) Ligand-
722 induced internalization and recycling of the human neuropeptide Y2 receptor is
723 regulated by its carboxyl-terminal tail. *J Biol Chem* **285:** 41578-90.
724 Wanka L, Babilon S, Kaiser A, Mörl K, Beck-Sickinger AG (2018) Different mode of arrestin-
725 3 binding at the human Y(1) and Y(2) receptor. *Cell Signal* **50:** 58-71.
726 Wawrezinieck L, Rigneault H, Marguet D, Lenne PF (2005) Fluorescence correlation
727 spectroscopy diffusion laws to probe the submicron cell membrane organization.
728 *Biophys J* **89:** 4029-42.
729 Wootten D, Christopoulos A, Marti-Solano M, Babu MM, Sexton PM (2018) Mechanisms of
730 signalling and biased agonism in G protein-coupled receptors. *Nat Rev Mol Cell Biol* **19:**
731 638-53.
732 Ziffert I, Kaiser A, Babilon S, Mörl K, Beck-Sickinger AG (2020) Unusually persistent Gα(i)-
733 signaling of the neuropeptide Y(2) receptor depletes cellular G(i/o) pools and leads to a
734 G(i)-refractory state. *Cell Commun Signal* **18:** 49.

735

Figures

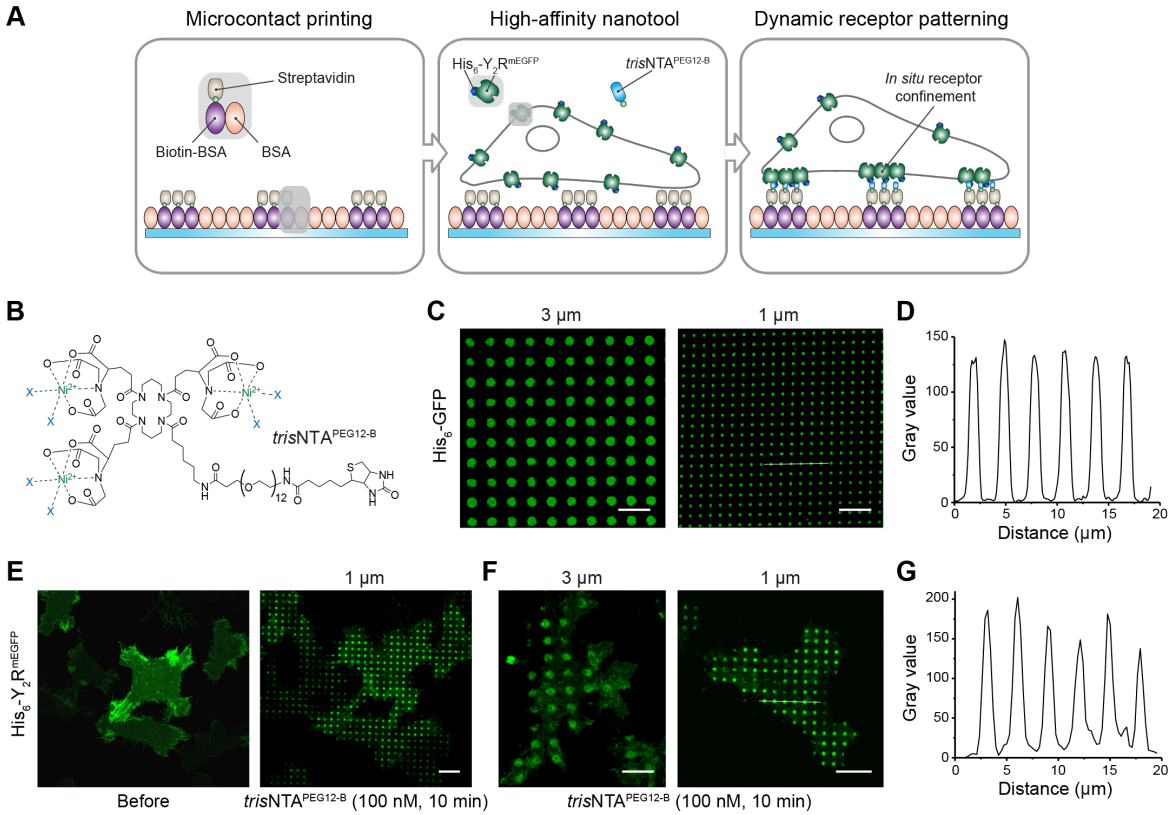

Figure 1. High-content ligand-free receptor confinement.

A Rational of the high-content ligand-free receptor clustering. Matrices prestructured with BSA are stepwise functionalized with biotin-BSA and SA. Upon addition of the multivalent nanotool *tris*NTA$^{PEG12-B}$, His_6-tagged receptors in HeLa cells are captured to the prestructured regions via the His-tag/*tris*NTA interaction.

B Chemical structure of the *tris*NTA$^{PEG12-B}$.

C Variable size protein patterns generated by further functionalization of SA-matrices with the nanotool followed by incubation with His_6-GFP (0.1 µM, 20 min). Images were acquired by confocal laser scanning microscopy.

D Intensity profile of the 1 µm pattern (white line in C) reflects high specificity of the interaction.

E Large-scale cell patterning in living cells occurred after addition of the *tris*NTA$^{PEG12-B}$ (100 nM, 10 min).

F Customized Y_2R assembly on 3 µm and 1 µm SA-prestructured matrices.

752 G Intensity profile of the 1 μm pattern (white line in f) showed an intensity comparable to a

753 soluble His_6-tagged protein. Scale bars: 10 μm.

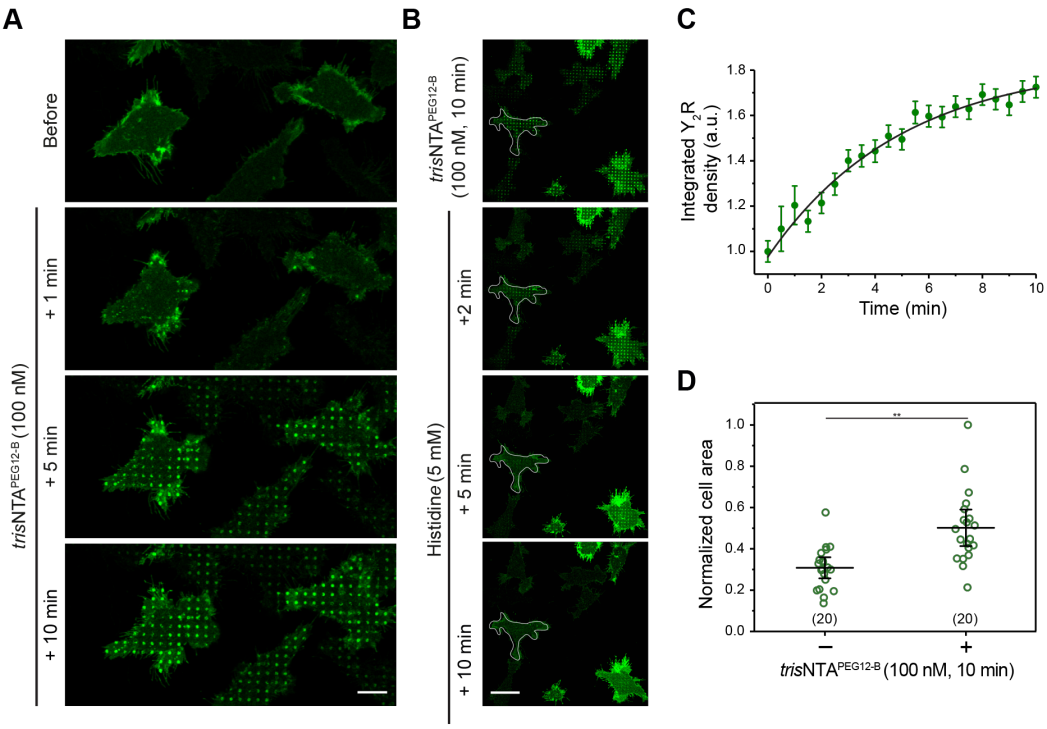

754

755 **Figure 2. Ligand-independent response triggered by *in situ* receptor confinement.**

756 A Time-lapse imaging of Y_2R assembly. Y_2R expressing HeLa cells were allowed to adhere
757 to prestructured SA-matrices for 3 h and visualized by CLSM in LCIS at 37 °C. Time-lapse
758 images were recorded for 10 min immediately after addition of *tris*NTA$^{PEG12-B}$ (100 nM).

759 B Reversal of the interaction and disassembly of the clusters is demonstrated upon addition
760 of histidine. Y_2R expressing cells were allowed to adhere to the SA-matrices for 3 h, and
761 then receptor confinement was induced by addition of *tris*NTA$^{PEG12-B}$ (100 nM).
762 Subsequently, cells were incubated with histidine (5 mM) for 2 to 10 min followed by
763 washing.

764 C Receptor integrated density in the patterned regions increased mono-exponentially, leading
765 to an assembly rate of 0.20 ± 0.03 min^{-1} and $\tau_{1/2}$= 5 min.

766 D Fast cell spreading upon cluster formation was observed. Cell area analysis before and
767 10 min after nanotool addition showed a 20% area increase, confirming an effect of the
768 receptor clusters on cell response. Values for cell area were normalized with respect to the
769 highest value. The mean ± SD (20 cells) is shown. **p≤ 0.01 for Tukey test. Scale bars:
770 10 µm.

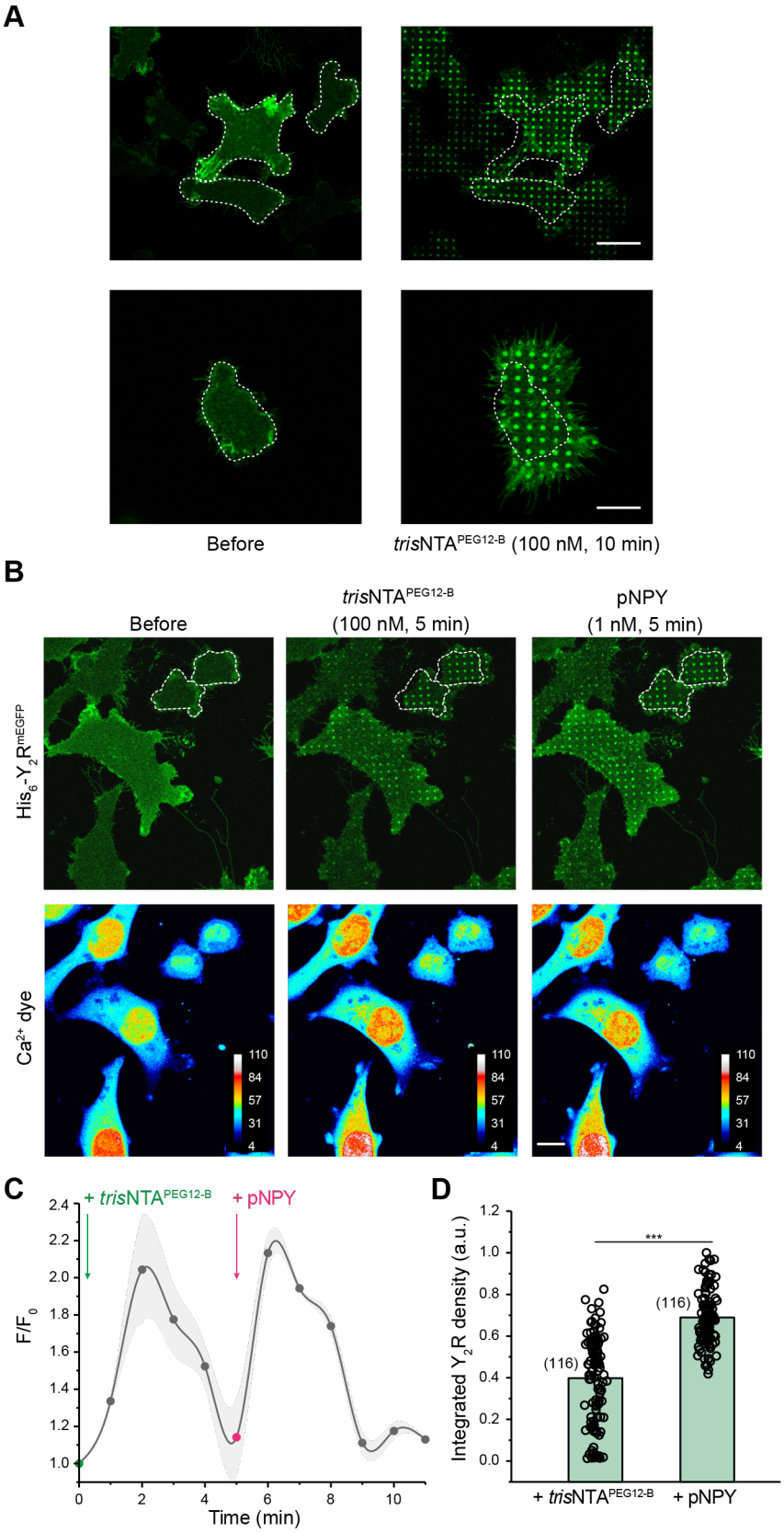

Figure 3. Ligand-free receptor confinement triggers calcium signaling.

773 A Representative images of His_6-Y_2R^{mEGFP} expressing cells over SA-prestructured matrices
774 before and in the presence of *tris*NTA$^{PEG12-B}$ demonstrated a significant change in cell area.
775 Scale bar: 20 µm upper panel, 10 µm lower panel.
776 B Representative fluorescence images of the Y_2R (upper panel) and color-coded images of
777 the Ca^{2+} dye (lower panel). Y_2R expressing cells on SA-prestructured matrices were
778 incubated with BioTracker 609 Red Ca^{2+} AM dye (3 µM) for 30 min. After rinsing, cells were
779 immediately imaged by CLSM in LCIS at 37 °C. Addition of the nanotool showed a twofold
780 increase in cytosolic calcium.
781 C Analysis of the mean gray value for Ca^{2+} signal before (F_0) and upon addition of
782 *tris*NTA$^{PEG12-B}$ (F) *versus* time. Time-lapse images were recorded with 45 s interval before
783 and after addition of *tris*NTA$^{PEG12-B}$ (100 nM) (5 slices z-stack per time-point). ROIs covering
784 the complete cell area were considered. The mean ± SD (10 cells) is shown. Scale bar:
785 10 µm.
786 D Quantification of receptor integrated density in the nanotool patterned regions showed an
787 increase in the density of the receptors within the clusters after addition of the pNPY. The
788 mean ± SD is shown (113 1 µm ROI were analyzed). ***$p \leq 0.001$ for Tukey test.

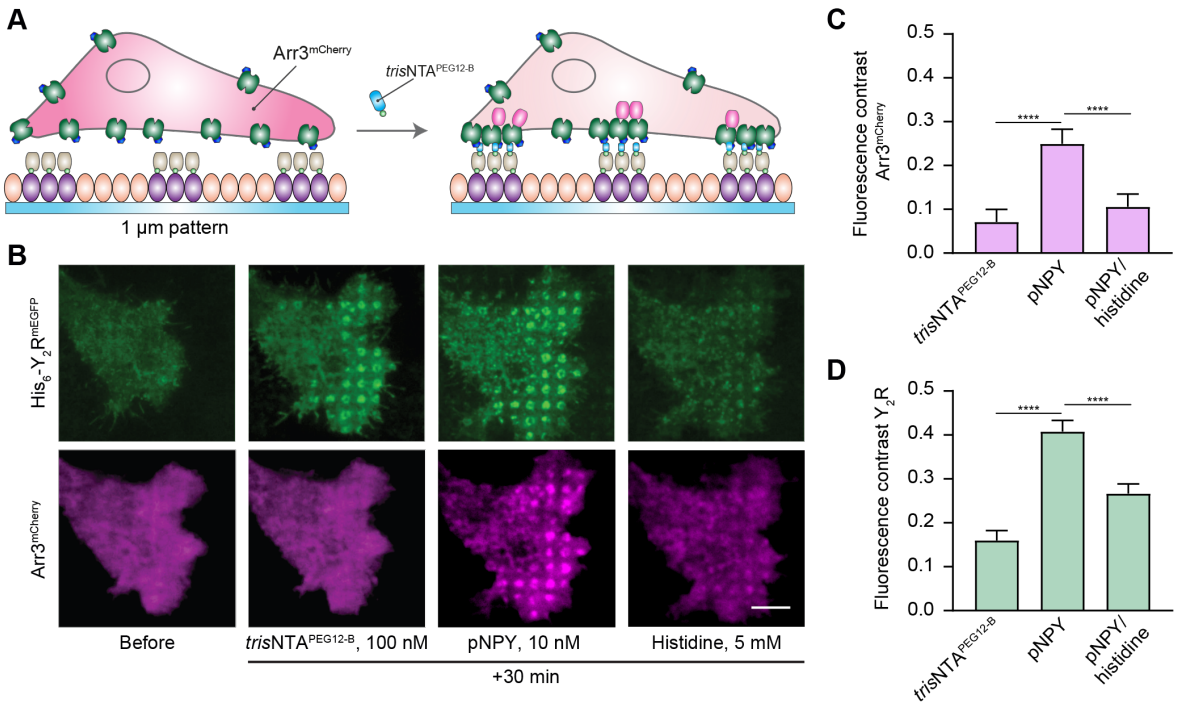

Figure 4. Selective arrestin-3 recruitment upon ligand-induced receptor activation.

A Schematic representation of the experimental set-up. Cells co-expressing Y_2R and Arr3 were allowed to adhere to SA-prestructured matrices for 3 h and visualized by total internal reflection fluorescence (TIRF) microscopy in LCIS at 37 °C.

B Representative TIRF images of cells before and upon addition of *tris*NTA$^{PEG12-B}$ (100 nM, 30 min) and subsequent incubation with porcine neuropeptide pNPY (10 nM) and Histidine (5 mM) in LCIS for 30 min at 37 °C. Scale bar: 5 µm.

C Fluorescence contrast analysis demonstrated no significant recruitment of Arr3 upon *tris*NTA$^{PEG12-B}$ (1.4-fold with respect to the basal signal before, 100 nM, 30 min). Addition of pNPY increased Arr3 signal (3.6-fold, 10 nM, 30 min) confirming co-patterning of the downstream signaling molecule. Subsequent addition of histidine led to a decrease in the signal (2.3-fold, 5 mM, 30 min). Data was normalized with respect to the fluorescence intensity before clustering and it is expressed as the means ± SEM (60 cells for each condition were analyzed). Tukey's multiple comparisons test was applied (***$p \leq 0.001$)

D Quantification of the fluorescence contrast in the patterned regions for Y_2R confirmed receptor enrichment upon addition of *tris*NTA$^{PEG12-B}$, (2-fold with respect to the basal signal

806 before, 100 nM, 30 min) which further increased 4-fold upon addition of pNPY (10 nM, 30
807 min). Histidine addition led to a decrease in the signal (1.7-fold decrease compared to
808 pNPY, 5 mM, 30 min). Data was normalized with respect to the fluorescence intensity
809 before clustering and it is expressed as the means ± SEM (60 cells for each condition were
810 analyzed). Tukey's multiple comparisons test was applied (***$p \leq 0.001$).

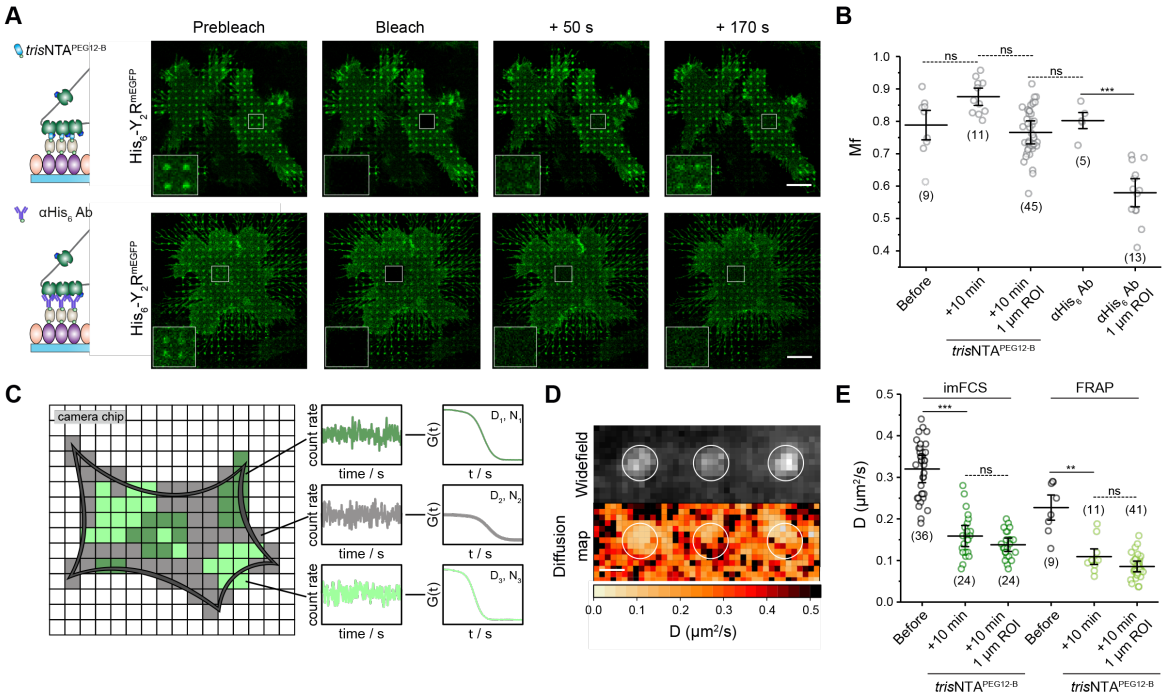

Figure 5. Decrease of receptor mobility in confined regions.

A Confocal images of FRAP measurements upon Y_2R clustering induced either by the nanotool *in situ* or by an anti-His_6 antibody. Insets represent the bleached ROIs. Fast recovery of the clusters can be detected for the case of the multivalent nanotool.

B Quantification of the receptor mobile fraction for cell patterning by the *tris*NTA$^{PEG12-B}$ and anti-His_6 antibody demonstrated a significant decrease in the receptor mobile fraction for the antibody matrices suggesting a lower receptor exchange. The mean ± SD is shown. 9 cells before, 11 cells after *tris*NTA$^{PEG12-B}$ (45x 1 µm ROIs) and 5 cells on anti-His_6 antibody matrices (13x 1 µm ROIs) were analyzed. ***$p \leq 0.001$ for Tukey test.

C imFCS correlates fluorescence intensity fluctuations in single camera pixels with a large degree of statistics, providing accurate diffusion coefficients with high spatial and temporal resolution.

D Widefield image of a ROI at the plasma membrane of a living cell upon addition of the nanotool analyzed by imFCS (left). The analyses of numerous pixels simultaneously provide two-dimensional diffusion data that draw a picture of the mobility of membrane receptors and reveal local differences in the diffusion (right).

828 E Both techniques demonstrated a decrease in the lateral diffusion of the receptor at the
829 plasma membrane after addition of the nanotool. Analysis of 1 µm clusters within the entire
830 ROI led to a further decrease in the lateral diffusion coefficient. For imFCS analyses, two-
831 sample t-tests (α = 0.05) were applied to compare the diffusion coefficients for the different
832 conditions. The mean ± SD is shown. 36 and 24 cells for the conditions before and after
833 addition of *tris*NTA$^{PEG12-B}$ were analyzed. For FRAP, the mean ± SD is shown (9 cells
834 before, 11 cells after *tris*NTA$^{PEG12-B}$, 41 1 µm ROIs were analyzed). ***p≤ 0.001 for Tukey
835 test. Scale bar: 10 µm (A), 1 µm (D).

836 **Expanded View Figures**

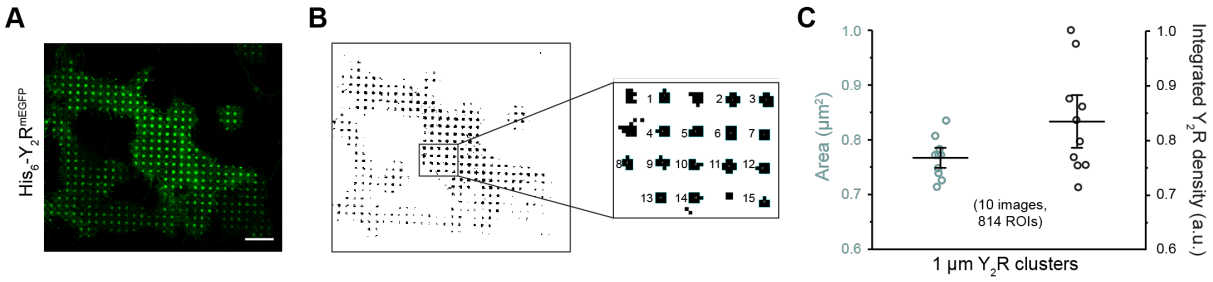

837

838 **Figure EV1. Receptor confinement with high reliability**.

839 A Representative confocal image of a cell patterned by *tris*NTA$^{PEG12-B}$ (100 nM).

840 B Automatic cluster analysis performed by ImageJ requires a "binary", black and white,
841 image. A threshold range is set to select the objects of interest apart from the background.
842 All pixels in the image whose values lie under the threshold are converted to white and all
843 pixels with values above the threshold are converted to black. Further selection of the
844 clusters according to area and roundness enable a large-scale analysis.

845 C Change in cluster area and integrated density of the receptor within different 96-well plates,
846 different months and cell stocks reflected a reliable and reproducible approach. The
847 average area in the clustered regions (0.77 ± 0.03 µm^2) and integrated density of ten
848 images in five different experiments (841x ROIs of 1 µm in total) is shown. Scale bar:
849 10 µm.

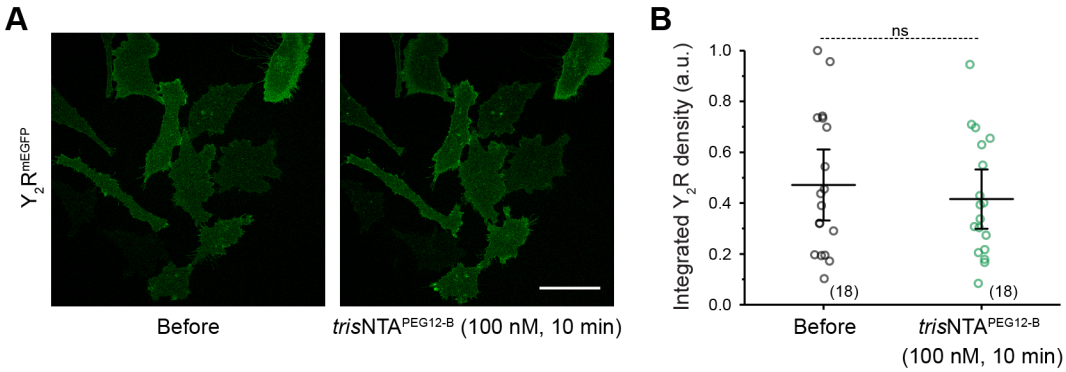

Figure EV2. Y_2 receptors lacking a His_6-tag do not cluster in confined areas.

A Cells expressing Y_2 receptors without N-terminal His_6-tag over SA-prestructured matrices before and after addition of the nanotool. Within the timeframe of imaging, there was neither a pattern formation nor a change in the integrated receptor density.

B Quantification of the integrated Y_2R density before and after addition of *tris*NTA$^{PEG12-B}$. The mean ± SD (18 cells) is shown. **$p \leq 0.01$ for Tukey test. Scale bar: 50 µm.

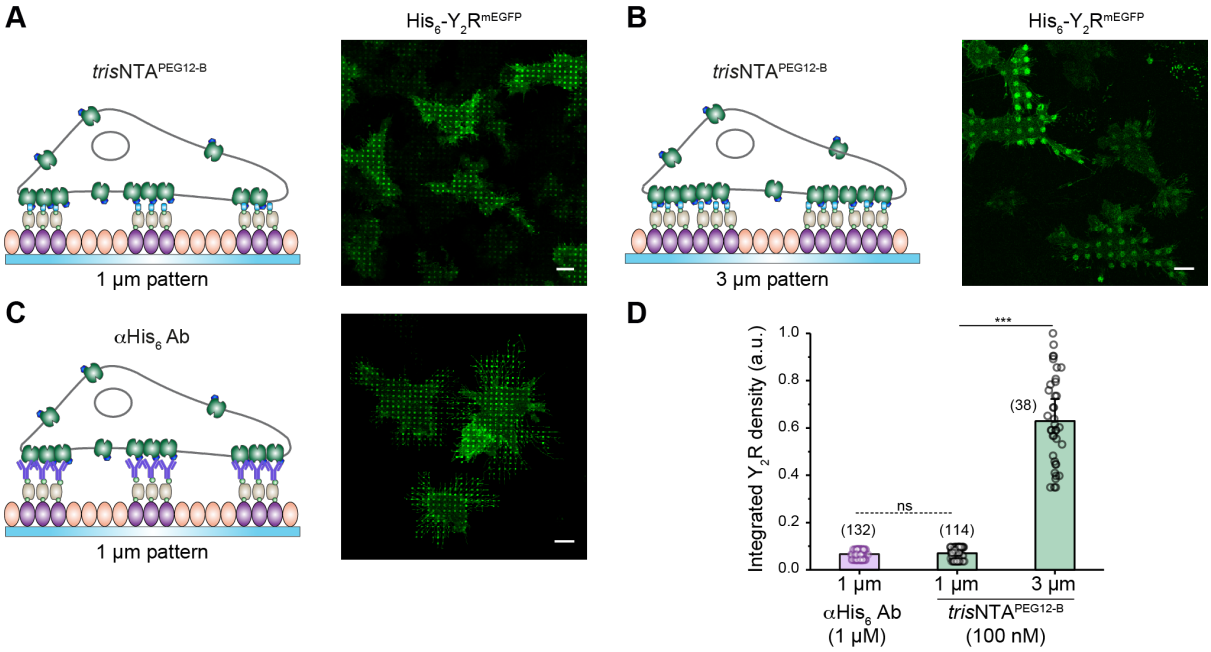

Figure EV3. Receptor density correlates with the area of the prestructured regions.

A,B BSA-prestructured matrices (1 µm, A or 3 µm, B) were stepwise functionalized with biotin-BSA and SA. Y_2R expressing HeLa cells were allowed to adhere to the functionalized matrix for 3 h and immediately imaged by CLSM in live-cell imaging solution (LCIS) at 37 °C. Addition of *tris*NTA$^{PEG12-B}$ (100 nM) led to *in situ* receptor assembly.

C 1 µm BSA-prestructured matrices were stepwise functionalized with biotin-BSA, SA, and a biotinylated anti-His_6 antibody (αHis_6 Ab). Y_2R expressing cells were allowed to adhere to the functionalized matrix for 3 h and immediately imaged by CLSM in LCIS at 37 °C.

D Quantification of the receptor integrated density. *In situ* receptor confinement by *tris*NTA$^{PEG12-B}$ resulted in a receptor density, which is comparable to cells in contact with prestructured antibodies. For the 3 µm patterns, receptor density correlated with pattern area. The mean ± SD (38 to 132x ROIs of 1 µm) is shown. ***$p \leq 0.001$ for Tukey test. Scale bars: 10 µm.

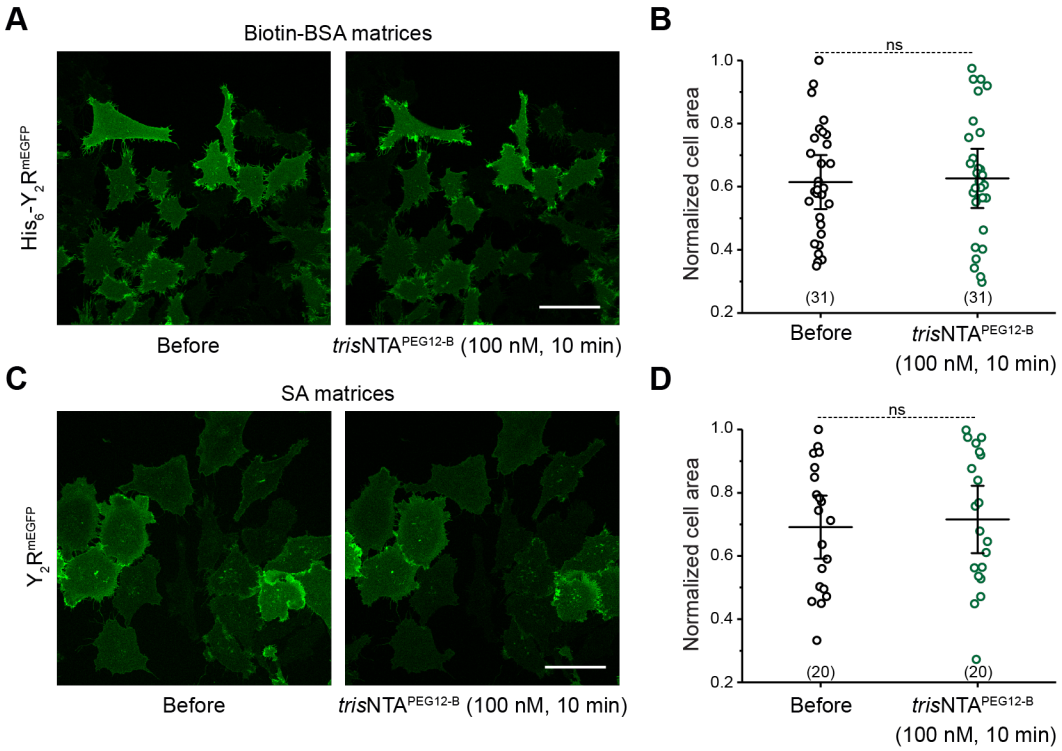

Figure EV4. Changes in cell motility are exclusively triggered upon receptor clustering.

A,B Confocal images of cells expressing His_6-tagged Y_2R on matrices which do not contain SA but only biotin-BSA. Addition of the *tris*NTA$^{PEG12-B}$ nanotool confirms no effect on cell spreading and motility as shown in the quantification of the cell area (B). The mean ± SD (31 cells) is shown. **p≤ 0.01 for Tukey test.

C Confocal images of cells expressing Y_2 receptors lacking the His_6-tag on SA-matrices do not present significant changes in cells spreading upon addition of the nanotool.

D Quantification of the cell area before and after addition of *tris*NTA$^{PEG12-B}$ (100 nM). Values for cell area were normalized with respect to the highest value. The mean ± SD (20 cells) is shown. **p≤ 0.01 for Tukey test. Scale bar: 50 µm.

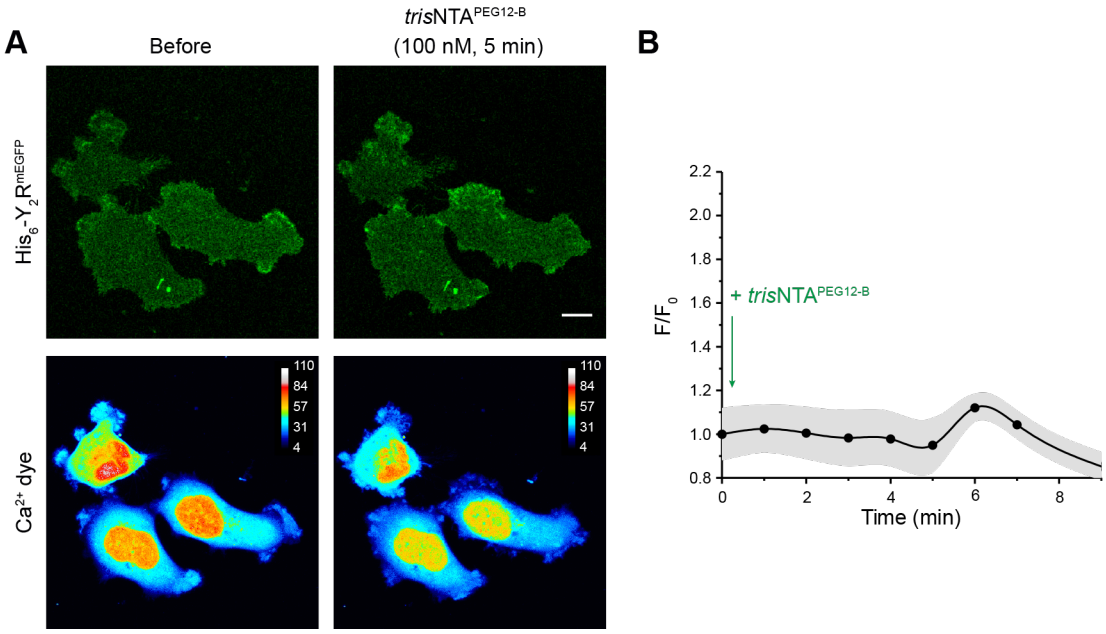

882

883 **Figure EV5. Calcium signaling is a specific response upon clustering.**

884 A Representative fluorescence images of the Y_2R (upper panel) and color-coded images of
885 the Ca^{2+} dye (lower panel). Y_2R expressing cells over prestructured matrices in absence of
886 streptavidin were incubated with BioTracker 609 Red Ca^{2+} AM dye (3 µM) for 30 min. After
887 rinsing, cells were immediately imaged by CLSM in LCIS at 37 °C. Addition of *tris*NTA^{PEG12-}
888 ^{B} showed neither clustering nor change in cytosolic calcium. Scale bar: 10 µm

889 B Analysis of the mean gray value for Ca^{2+} signal before (F_0) and upon addition of
890 *tris*NTA$^{PEG12-B}$ (F) *versus* time. Time-lapse images were recorded with 45 s interval before
891 and after addition of *tris*NTA$^{PEG12-B}$ (100 nM) (5 slices z-stack per time-point). ROIs covering
892 the complete cell area were considered. The mean ± SD (10 cells) is shown.

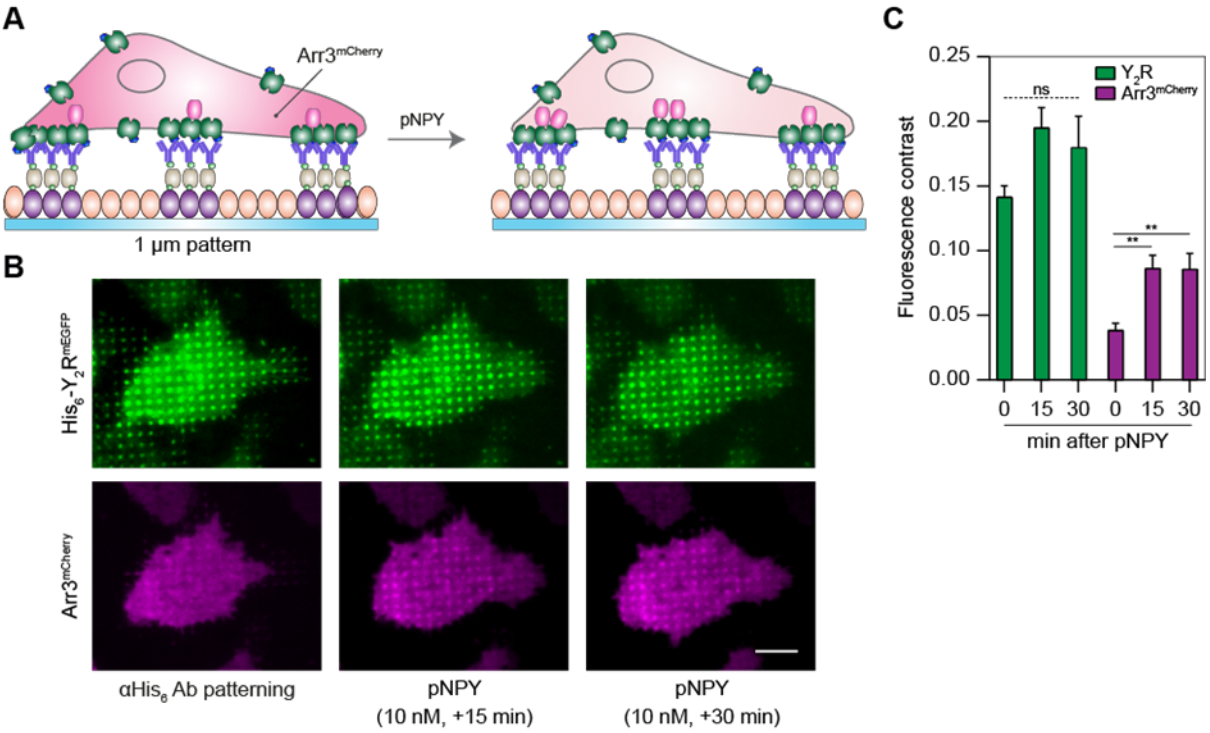

Figure EV6. Arrestin-3 recruitment on antibody-confined regions.

A Schematic representation of the experimental set-up. Cells co-expressing Y_2R and Arr3 were allowed to adhere to anti-His_6 antibody prestructured matrices for 3 h and visualized by total internal reflection fluorescence (TIRF) microscopy in LCIS at 37 °C.

B Representative TIRF images of cells before and upon addition of pNPY (10 nM) in LCIS for 30 min at 37 °C. Scale bar: 10 µm.

C Quantification of the fluorescence contrast in the Y_2R-patterned regions showed no significant change in receptor intensity yet a recruitment of Arr3 upon addition of pNPY (twofold). Data are expressed as the means ± SEM (30 cells for each condition were analyzed). Tukey's multiple comparisons test was applied (**$p \leq 0.01$).

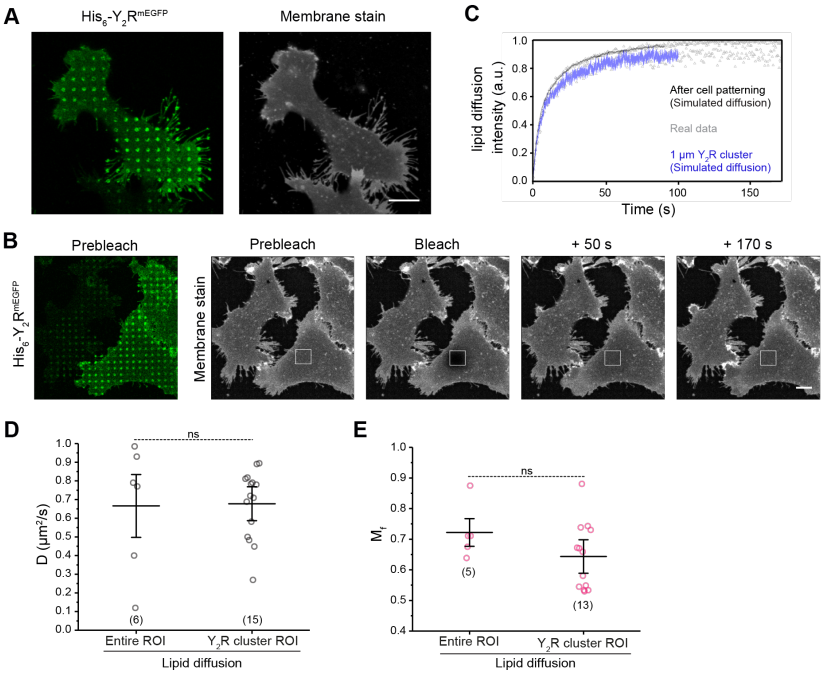

Figure EV7. Lipid localization and dynamics after receptor confinement.

A Live-cell plasma membrane staining was performed 15 min after Y_2R assembly in living cells. 5 µg/ml CellMask staining solution was incubated for 5 min at 37 °C and washed with LCIS before visualization. Lipid distribution is not affected by receptor confinement as shown by the homogeneous staining of the membrane.

B Representative confocal images of FRAP measurements for the lipid dye. An image of the receptor channel confirmed the presence of the pattern.

C FRAP recovery for the lipid dye measured in the entire rectangular ROI or at the Y_2R cluster spots (region selected based on the receptor channel image) demonstrated a rapid recovery for the lipids.

D The analysis did not show any differences in lipid diffusion coefficients for the entire rectangular ROI or at the 1 µm clustered regions ($D_{\text{entire ROI}}$ = 0.66 ± 0.10 µm²/s and D_{spots} = 0.67 ± 0.17 µm²/s). The mean ± SD (6 cells, 15x 1 µm ROIs) is shown. **p≤ 0.01 for Tukey test.

E E Quantification of the mobile fraction (M_f) for FRAP measurements of the lipid dye reflected no significant difference. The mean ± SD (5 cells, 14x 1 µm ROIs) is shown. **p≤ 0.01 for Tukey test. Scale bars: 10 µm.

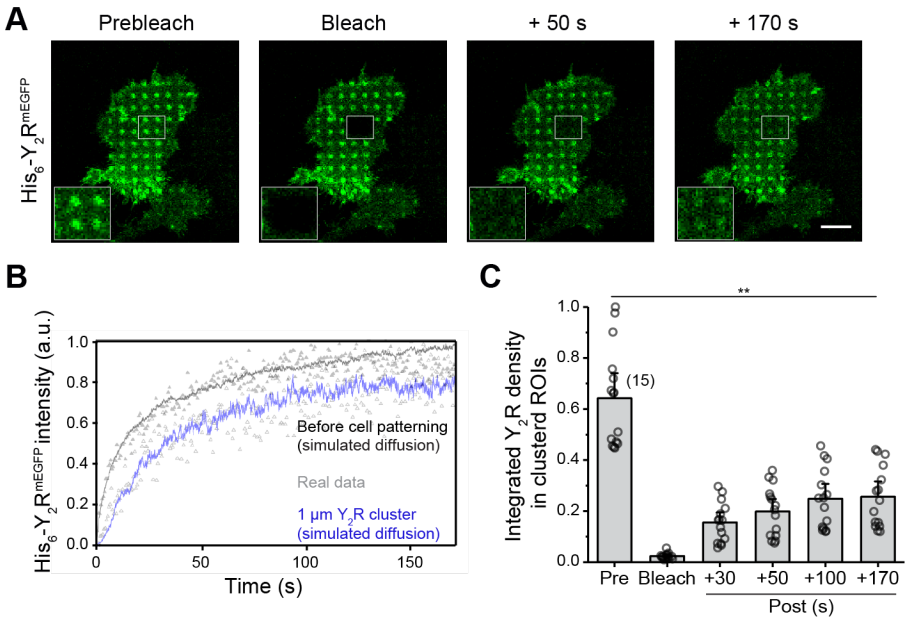

Figure EV8. Dynamic receptor exchange in confined clusters.

A Representative confocal images of FRAP measurements for Y_2R expressing cells on SA-prestructured matrices 10 min after addition of the nanotool.

B FRAP recovery curves reflecting the entire bleached area or an analysis performed only in the clustered 1 µm regions. The analysis is based on a simulation approach which fits a computer-simulated recovery to actual recovery data of a FRAP series and determines the diffusion coefficient regardless of bleaching geometry.

C Quantification of the receptor density in the confined regions showed 50% recovery indicating a high exchange rate. The mean ± SD (6 cells, 15x 1 µm ROIs analyzed) is shown. **$p \leq 0.01$ for Tukey test. Scale bar: 10 µm.

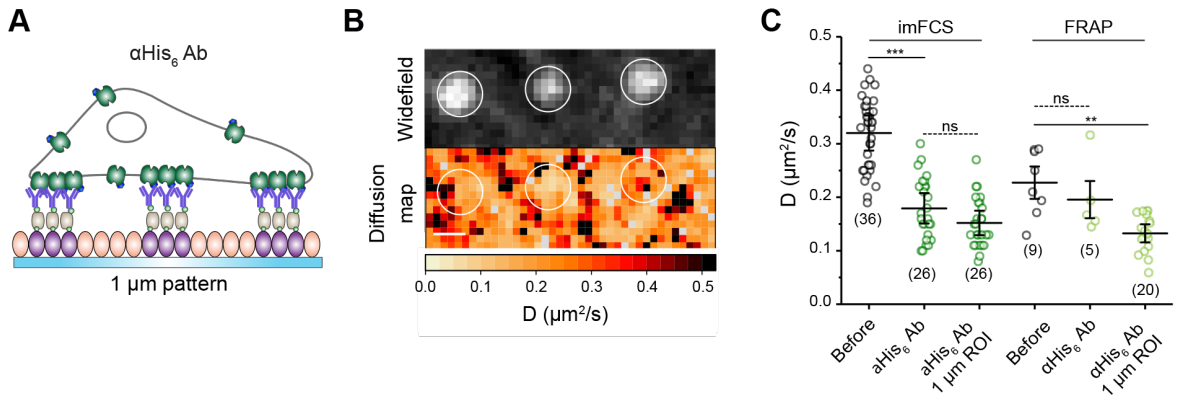

Figure EV9. Receptor mobility on antibody structured matrices.

A Scheme representing the experimental set-up.

B Representative widefield image (left) of a ROI at the plasma membrane of a living cell grown on prestructured matrices with an anti-His_6 antibody (αHis_6 Ab) analyzed by imFCS and the derived two-dimensional diffusion map (right).

C Lateral diffusion of the receptor analyzed by FRAP and imFCS. Both techniques demonstrated a decrease in D at the plasma membrane (D_{before}= 0.32 ± 0.06 µm²/s and 0.25 ± 0.08 µm²/s; $D_{\text{anti-His6 Ab}}$ = 0.18 ± 0.06 and 0.19 ± 0.06 µm²/s for imFCS and FRAP respectively), concurring with the values obtained for the measurements upon addition of the nanotool. Analysis of clustered regions (1 µm) within the selected ROIs led to a further decrease in the diffusion coefficient (D_{spots}= 0.15 ± 0.05 µm²/s and 0.13 ± 0.03 µm²/s for imFCS and FRAP, respectively). For imFCS measurements, two-sample t-tests (α = 0.05) were applied to compare the diffusion coefficients for the different conditions (***p≤ 0.001). The mean ± SD is shown. 36 and 26 cells for the conditions before and after addition of anti-His_6 antibody were analyzed. For FRAP, the mean ± SD is shown. Here, 9 cells before, 5 cells after addition of anti-His_6 antibody, 20x ROIs were examined. **p≤ 0.01 for Tukey test. Scale bar: 1 µm.

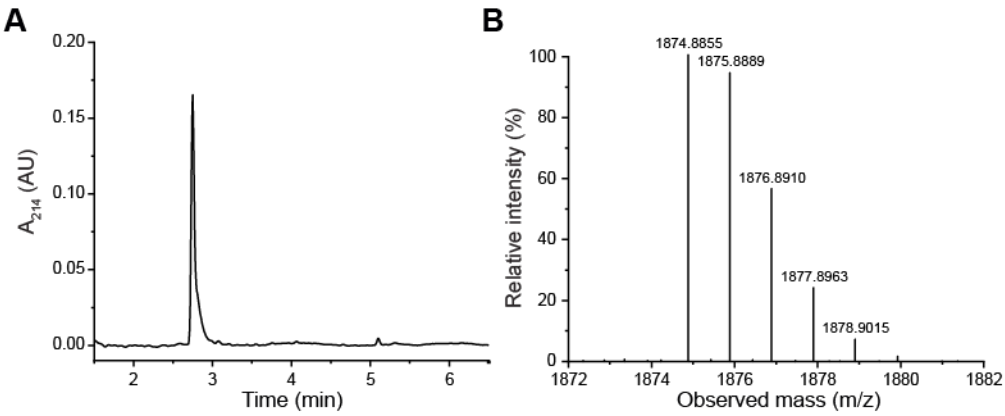

Figure EV10. Multivalent nanotool *tris*NTA$^{PEG12-B}$ analyzed by LC-MS.

A *tris*NTA$^{PEG12-B}$ chromatogram reflecting the purity of the synthesized nanotool.

B LC-MS of *tris*NTA$^{PEG12-B}$, yielding the experimental mass ($M_{exp.}$) of 1874.85 Da ($M_{theor.}$ = 1873.90 Da).